

Madden–Julian Oscillation Pacific Teleconnections: The Impact of the Basic State and MJO Representation in General Circulation Models

STEPHANIE A. HENDERSON AND ERIC D. MALONEY

Department of Atmospheric Science, Colorado State University, Fort Collins, Colorado

SEOK-WOO SON

School of Earth and Environmental Sciences, Seoul National University, Seoul, South Korea

(Manuscript received 3 November 2016, in final form 23 February 2017)

ABSTRACT

Teleconnection patterns associated with the Madden–Julian oscillation (MJO) significantly alter extratropical circulations, impacting weather and climate phenomena such as blocking, monsoons, the North Atlantic Oscillation, and the Pacific–North American pattern. However, the MJO has been extremely difficult to simulate in many general circulation models (GCMs), and many GCMs contain large biases in the background flow, presenting challenges to the simulation of MJO teleconnection patterns and associated extratropical impacts. In this study, the database from phase 5 of the Coupled Model Intercomparison Project (CMIP5) is used to assess the impact of model MJO and basic state quality on MJO teleconnection pattern quality, and a simple dry linear baroclinic model is employed to understand the results. Even in GCMs assessed to have good MJOs, large biases in the MJO teleconnection patterns are produced as a result of errors in the zonal extent of the Pacific subtropical jet. The horizontal structure of Indo-Pacific MJO heating in good MJO models is found to have modest impacts on the teleconnection pattern skill, in agreement with previous studies that have demonstrated little sensitivity to the location of tropical heating near the subtropical jet. However, MJO heating east of the date line can alter the teleconnection pathways over North America. Results show that GCMs with poor basic states can have equally low skill in reproducing the MJO teleconnection patterns as GCMs with poor MJO quality, suggesting that both the basic state and the MJO must be well represented in order to reproduce the correct teleconnection patterns.

1. Introduction

The importance of the Madden–Julian oscillation (MJO) to the global circulation has been widely investigated since its first detection in the early 1970s (Madden and Julian 1971, 1972). The MJO is an intraseasonal tropical convectively coupled disturbance that propagates eastward from the western Indian Ocean to the central Pacific Ocean over a period of approximately 30–90 days. During an MJO event, anomalous convection acts as a tropical heat source emitting stationary Rossby waves that propagate into the extratropics and significantly modulate the extratropical circulation (e.g., Matthews et al. 2004; Seo and Son 2012). The MJO modulates various aspects of weather and climate including regional temperatures (e.g., Vecchi and Bond 2004), precipitation

(e.g., Jones et al. 2004; Donald et al. 2006), atmospheric blocking (e.g., Henderson et al. 2016), hurricanes (e.g., Maloney and Hartmann 2000; Liebmann et al. 1994), and global monsoons (Lorenz and Hartmann 2006; Lau and Waliser 2012), as well as important modes of climate variability such as the North Atlantic Oscillation (NAO; e.g., Cassou 2008; Lin et al. 2009) and the Pacific–North American (PNA) pattern (e.g., Mori and Watanabe 2008; Riddle et al. 2013). The widespread influence of the MJO implies that accurate prediction of global circulation patterns and weather events requires consideration of MJO activity and its accurate simulation in climate and weather forecasting models.

Although its global influence is substantial, the MJO has been difficult to properly simulate in general circulation models (GCMs; e.g., Kim et al. 2009, 2011; Hung et al. 2013). The overall representation of the MJO in GCMs has been improved since phase 3 of the Coupled Model Intercomparison Project (CMIP3), the international

Corresponding author e-mail: Stephanie A. Henderson, sslade1@atmos.colostate.edu

collaboration of GCMs that played a key role in the Fourth Assessment Report (AR4) of the Intergovernmental Panel on Climate Change (IPCC). In particular, model improvements for phase 5 of the CMIP project (CMIP5) have led to improved MJO spectral characteristics in equatorial precipitation and zonal wind as well as increased MJO variance. However, many state-of-the-art GCMs still exhibit severe deficiencies in simulating the MJO, including unrealistically short MJO persistence and poor or nonexistent eastward propagation of MJO convection (e.g., [Ahn et al. 2017](#); [Jiang et al. 2015](#); [Kim et al. 2014](#); [Hung et al. 2013](#)).

Errors in MJO simulations can introduce systematic errors in extratropical circulations. Previous studies have shown that tropical thermal forcing, such as that associated with anomalous MJO convection, is balanced by ascending motion and divergent winds aloft. This upper-tropospheric divergent flow generates upper-level anticyclonic anomalies that can produce stationary Rossby waves that extend into higher latitudes (e.g., [Hoskins and Karoly 1981](#)). The location and amplitude of the Rossby waves is dependent on the location, amplitude, and structure of the heat source (e.g., [Hoskins and Karoly 1981](#); [Jin and Hoskins 1995](#); [Yasui and Watanabe 2010](#)). This suggests that errors in MJO simulations can influence the nature of Rossby waves emitted by MJO heating and the associated circulation anomalies that impact the extratropics. Model MJO teleconnections are further complicated by the accuracy of the model basic state. The background flow determines the direction and propagation characteristics of MJO-induced Rossby waves (e.g., [Hoskins and Ambrizzi 1993](#); [Ting and Sardeshmukh 1993](#)). However, a key issue is that improvements in the representation of the MJO in GCMs often negatively impact the basic state ([Kim et al. 2011](#)). All else being equal, modelers may prefer a realistic basic state rather than a more realistic MJO when deciding on the suite of parameterizations to use in their climate models. This problem may explain why little focus has been given to MJO teleconnections in GCMs, which require an accurate representation of both the mean state and MJO.

Recent studies have demonstrated that the ability of GCMs to reproduce teleconnection patterns associated with tropical variability depends on both the model basic state (e.g., [Dawson et al. 2011](#)) and the quality of the heating (e.g., [Yoo et al. 2015](#)). For example, improvements to the basic state due to increased resolution have been shown to improve the accuracy of the teleconnection patterns associated with the El Niño–Southern Oscillation (ENSO) in the High-Resolution Global Environmental Model, version 1.2 (HiGEM1.2; [Dawson et al. 2011](#)). [Weare \(2013\)](#) noted that the

teleconnection patterns associated with ENSO warm events are influenced by the quality of upper-tropospheric flow anomalies associated with ENSO heating and the length and frequency of ENSO events. By examining the influence of convection schemes on the model MJO and associated Rossby wave pathways in the Community Atmosphere Model, version 5 (CAM5), [Yoo et al. \(2015\)](#) found that using a unified convection scheme rather than the default deep and shallow convection schemes resulted in improved MJO characteristics and more realistic MJO teleconnection patterns. Furthermore, the study noted that little is known about the behavior of MJO teleconnections in GCMs.

Given the significant impact of the MJO on the extratropical circulation, it is important to quantify how model MJO and basic state errors impact the MJO teleconnection patterns in GCMs. This exercise may provide insight into possible causes of simulation errors in extratropical weather and climate that are known to be significantly modulated by the MJO. In climate change studies, MJO teleconnection errors may introduce uncertainties in future projections of extreme weather events and climate patterns that are significantly modulated by the MJO. Hence, it is important that modelers and climate scientists are aware of these errors and the reasons for them.

This study examines the MJO teleconnection patterns of 10 CMIP5 models with a focus on the role of the model MJO and basic state quality on MJO teleconnection patterns. The CMIP5 models and reference datasets are described in [section 2](#), as well as a description of the general methodology of the study. [Section 3](#) investigates the ability of the CMIP5 models to correctly simulate the MJO, basic state, and the MJO teleconnection patterns. In [section 4](#), a linear baroclinic model (LBM) is employed to analyze the individual impacts of the model MJO and basic state performance on the quality of MJO teleconnection patterns. Last, a summary and conclusions are provided in [section 5](#).

2. Methodology

a. Model and observational data

The 10 CMIP5 models examined are listed in [Table 1](#). The GCMs selected for this study have varying degrees of MJO quality and basic state performance, useful for the purposes of this study. As a side note, additional CMIP5 model data were unavailable at the time of our investigations owing to problems with the CMIP5 website. The analysis performed here was therefore not extended beyond the 10 models initially chosen for this

TABLE 1. CMIP5 models evaluated and their corresponding institution and horizontal resolution. Models determined to have a relatively good MJO are in bold.

	Model	Institution	Resolution
1	BCC_CSM1.1	Beijing Climate Center, China	$2.8^\circ \times 2.8^\circ$
2	CanESM2	Canadian Centre for Climate Modelling and Analysis, Canada	$2.8^\circ \times 2.8^\circ$
3	CNRM-CM5	Centre National de Recherches Météorologiques, France	$1.4^\circ \times 1.4^\circ$
4	GFDL CM3	NOAA/Geophysical Fluid Dynamics Laboratory	$2^\circ \times 2.5^\circ$
5	GFDL-ESM2G	NOAA/Geophysical Fluid Dynamics Laboratory	$2^\circ \times 2.5^\circ$
6	GFDL-ESM2M	NOAA/Geophysical Fluid Dynamics Laboratory	$2^\circ \times 2.5^\circ$
7	IPSL-CM5A-MR	L'Institut Pierre-Simon Laplace, France	$1.25^\circ \times 2.5^\circ$
8	MIROC5	Atmosphere and Ocean Research Institute (AORI), National Institute for Environmental Studies (NIES), and JAMSTEC, Japan	$1.4^\circ \times 1.4^\circ$
9	MRI-CGCM3	Meteorological Research Institute, Japan	$1.1^\circ \times 1.1^\circ$
10	NorESM1-M	Norwegian Climate Centre, Norway	$1.9^\circ \times 2.5^\circ$

study. Model output is taken from the first ensemble member of the CMIP5 historical runs, which use the observed evolution of forcing for the twentieth century (e.g., Taylor et al. 2012; Weare 2013). Unless otherwise stated, boreal winter [December–February (DJF)] monthly and daily model output is analyzed for December 1950–February 2005, for a total of 54 boreal winter seasons, with the exception of GFDL CM3, which only spans to 2004. The reference dataset used here is ERA-Interim (Dee et al. 2011). This dataset is provided on a $1.5^\circ \times 1.5^\circ$ grid and spans from December 1979 to February 2014, for a total of 34 winter seasons. Furthermore, daily winter precipitation observations from the Global Precipitation Climatology Project (GPCP; Adler et al. 2003) are used. The GPCP dataset spans from 1996 to 2015 and has a 1° grid spacing.

b. MJO indices

The eastward evolution of the MJO is represented using the real-time multivariate MJO (RMM) indices of Wheeler and Hendon (2004; <http://www.bom.gov.au/climate/mjo/>). The RMM indices (RMM1 and RMM2) are the first two principal components (PCs) of the combined empirical orthogonal functions (EOFs) of near-equatorially averaged (15°S – 15°N) anomalous outgoing longwave radiation (OLR) and 200- and 850-hPa zonal winds. The OLR data used to calculate the RMM indices are derived from NOAA satellite data and the winds from the NCEP–NCAR reanalysis (Wheeler and Hendon 2004). This definition of the MJO has been used in previous studies to examine the MJO teleconnection patterns and their associated extratropical impacts (e.g., Cassou 2008; Lin et al. 2009; Henderson et al. 2016).

To examine the model MJO teleconnections during the MJO life cycle, RMM indices are computed for each model by projecting the model equatorially averaged (15°S to 15°N) OLR and 250- and 850-hPa zonal winds onto the reanalysis EOFs, which were made available

by M. Wheeler (2015, personal communication). Projection onto the reanalysis EOFs allows for a consistent framework for comparison among the different model MJOs, including cases in which a model is not able to properly replicate the MJO EOFs but does contain some MJO-like variability (Waliser et al. 2009). More specifically, the model MJO indices are generated as follows: first, the mean of the previous 120 days is removed from the data to reduce the influence of interannual variability, and the first three harmonics of the seasonal cycle are removed. The three variables are then normalized by the reanalysis tropical standard deviation (based on all longitudes) of each corresponding field, provided by Matthew Wheeler, and projected onto the reanalysis EOFs. The RMM indices for each model are the resulting standardized PCs.

For all datasets, the time evolution of the MJO is represented by eight phases, where each phase is determined by $\tan^{-1}(\text{RMM2}/\text{RMM1})$, and provides an approximate longitudinal location of MJO convection. In this definition, MJO phase 1 indicates enhanced MJO convection in the western Indian Ocean, and MJO phase 8 is characterized by enhanced convection in the central Pacific. Composites relative to MJO phase are only generated when the MJO amplitude $\sqrt{(\text{RMM1}^2 + \text{RMM2}^2)}$ is greater than 1.

3. MJO teleconnections

The amplitude and direction of the stationary Rossby waves generated by tropical heating are dependent on two primary factors: 1) the location, amplitude, and structure of the thermal forcing and 2) the background flow into which the Rossby waves propagate (e.g., Hoskins and Karoly 1981; Jin and Hoskins 1995). The importance of these factors for producing realistic MJO teleconnections is assessed in this section. First, each model's ability to simulate the eastward propagation and

TABLE 2. J15 skill metric correlation coefficients, E/W ratio values, and areal-averaged tropical dry static stability values for observations/reanalysis and the CMIP5 models. Dry static stability values are provided only for the good MJO models.

Dataset	J15 skill metric			E/W ratio	$\delta\bar{s}/\partial p$
	Average	IO box	WP box		
GPCP/ERA-Interim	1.0	1.0	1.0	2.82	-0.45
BCC_CSM1.1	0.79	0.76	0.82	2.35	-0.44
CanESM2	0.70	0.70	0.70	0.94	—
CNRM-CM5	0.92	0.92	0.92	3.99	-0.35
GFDL CM3	0.86	0.86	0.87	1.89	-0.42
GFDL-ESM2G	0.74	0.80	0.68	1.48	—
GFDL-ESM2M	0.73	0.76	0.70	1.48	—
IPSL-CM5A-MR	0.68	0.67	0.70	1.59	—
MIROC5	0.85	0.82	0.89	1.99	-0.39
MRI-CGCM3	0.86	0.86	0.85	2.60	-0.44
NorESM1-M	0.91	0.89	0.93	2.09	-0.43

persistence of MJO heating is discussed. Based on three skill metrics, good MJO models are determined. Second, the differences in basic state from model to model and the resulting influence on Rossby wave propagation are examined. Last, the joint influence of model MJO quality and basic state quality on the ability to simulate MJO teleconnections is discussed.

a. Model MJO representation

Three diagnostics are used to determine which of the 10 models have a “good” MJO. The propagation characteristics of the model MJO are quantified by employing a diagnostic developed by the U.S. CLIVAR MJO working group (MJOWG; Waliser et al. 2009). Lagged correlations of the extended winter (April–November) intraseasonal (20–100 day) tropical (10°S–10°N) precipitation are used to create lag–longitude Hovmöller diagrams. Following Jiang et al. (2015), the lagged correlations are calculated relative to intraseasonal precipitation in the Indian Ocean (IO; 5°S–5°N, 75°–85°E) and the western Pacific (WP; 5°S–5°N, 130°–150°E) for lags of -20 to 20 days [see Fig. 4 of Ahn et al. (2017) for similar lag–longitude Hovmöller diagrams for all of the models used here]. The pattern correlations between the observed and GCM Hovmöller diagrams are then used to provide one metric for MJO skill (Jiang et al. 2015). The skill score, which we will refer to as the J15 skill score, is determined by taking the average of the pattern correlations derived for WP and IO reference points, with the “good” MJO models exceeding a 0.8 correlation with observations. The correlation values for WP and IO reference points and their average are provided in Table 2. Based on this skill score, CNRM-CM5, GFDL CM3, MIROC5, MRI-CGCM3, and NorESM1-M have a relatively good MJO.

Another commonly used skill metric developed by the MJOWG utilizes the extended winter wavenumber–frequency power spectrum of precipitation to assess the eastward- and westward-propagating components of the MJO (e.g., Waliser et al. 2009; Ahn et al. 2017). Precipitation output from GPCP and each GCM is averaged between 10°S and 10°N to calculate the power spectra in wavenumber–frequency space [not shown; see Fig. 1 of Ahn et al. (2017) for the precipitation power spectrum of all the models examined here]. The ratio of eastward to westward propagation power (E/W ratio) in the region containing zonal wavenumbers 1–3 and 30–60-day periods is then derived. The observed E/W ratio is 2.82, which is higher than most of the “good” MJO models (Table 2). Although BCC_CSM1.1 fell just short of the 0.8 J15 skill score threshold, it has a higher E/W ratio than some of the good MJO models and is therefore classified as a good MJO model here.

The ability for a model to maintain a high-amplitude MJO event once it is established is also considered. Following Rashid et al. (2011), MJO persistence is evaluated by using the two-dimensional phase space created by the RMMs (Fig. 1), where a strong MJO event is characterized by the counterclockwise evolution of the RMM indices with an amplitude greater than 1 (i.e., outside of the unit circle shown). The initial point of each trajectory, indicated by a large filled circle outside of the unit circle, represents the average RMM1 and RMM2 values for each quadrant in the RMM phase space for each model and reanalysis. The average MJO evolution beginning in each quadrant is shown for 16 days with the exception of CNRM-CM5 (light blue), which is shown for 51 days because of its strong persistence of high-amplitude behavior. MJO events in phases 1 and 2 (Fig. 1, bottom left quadrant) decay after an average of 14 days in ERA-Interim, where decay is defined as the last day the MJO amplitude remains above 1. This quadrant is associated with MJO initiation in the western Indian Ocean, indicating that on average observed MJO events do not persist for the full MJO life cycle of approximately 30–60 days, in agreement with Rashid et al. (2011). Model MJO evolution that decays within the same quadrant as its initial point indicates an inability of the model to maintain strong MJO amplitude (e.g., CanESM2, IPSL-CM5A-MR, GFDL-ESM2M, and GFDL-ESM2G). The average MJO event in these models are short-lived and likely developed within the same phase in which they decay. This behavior might also reflect non-MJO variability temporarily projecting onto observed RMM structures. In general, the MJO in the poor MJO models decays faster than that in the good MJO models for all

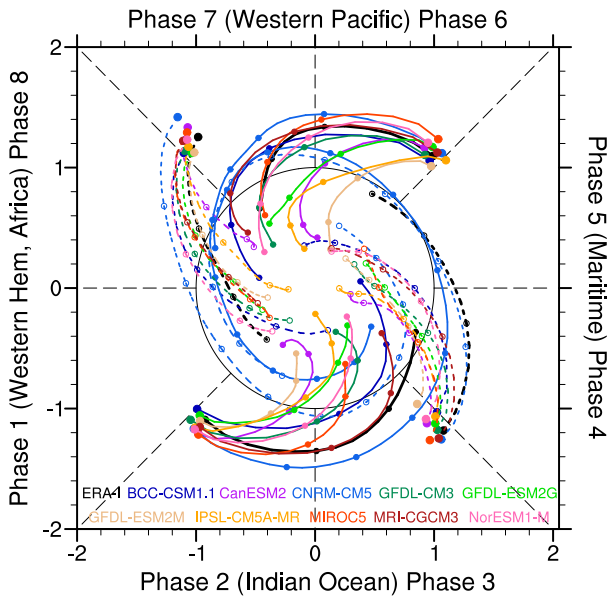


FIG. 1. RMM index amplitude trajectories in phase space for reanalysis (black line) and the CMIP5 models (colored lines; see legend). Trajectories initiate when each RMM index indicates a strong-amplitude MJO event (i.e., outside of the unit circle) in (counter-clockwise from bottom left) phases 1–2, phases 3–4, phases 5–6, and phases 7–8. Each trajectory is shown for 16 days, except for CNRM-CM5, which is shown for 51 days. Circles mark every five days. The composite RMM indices are smoothed with a five-point running mean prior to plotting as done by Rashid et al. (2011).

MJO phase quadrants. The three MJO skill diagnostics examined here generally agree on 6 of the 10 models having a good MJO (indicated in bold in Table 1), and these models will be referenced as such for the remainder of this study.

b. Model basic state

The characteristics of Rossby wave propagation are strongly influenced by the basic state. The dispersion of Rossby waves, as described in Hoskins and Ambrizzi (1993) and others, is largely determined by the mean upper-tropospheric zonal wind. The DJF-mean 250-hPa zonal winds for the good MJO models are shown in Fig. 2 (black contours), where the difference between each model and reanalysis is represented by the shaded color contours. Large errors in the strength, extent, and location of the mean Pacific subtropical jet are apparent in most of models shown. The subtropical jet in MRI-CGCM3, GFDL CM3, and MIROC5 extends too far east relative to reanalysis. Furthermore, a southward shift of the jet is apparent in MIROC5. NorESM1-M has the smallest mean zonal wind errors in the Pacific out of the models shown.

The large differences in the model upper-level zonal winds introduce significant biases in Rossby wave

propagation. Their possible impacts are discussed by utilizing the stationary wavenumber K_s on Mercator coordinates following Karoly (1983) and Hoskins and Ambrizzi (1993):

$$K_s = \left(\frac{a\beta_M}{\bar{u}_M} \right)^{1/2}, \tag{1}$$

where the Mercator zonal wind \bar{u}_M is the mean 250-hPa zonal wind divided by the cosine of latitude, and a is the radius of Earth. The meridional gradient of absolute vorticity on a sphere β_M is defined by

$$\beta_M = \frac{2\Omega \cos^2\theta}{a} - \frac{\partial}{\partial y} \left[\frac{1}{\cos^2\theta} \frac{\partial}{\partial y} (\cos^2\theta \bar{u}_M) \right], \tag{2}$$

where θ is latitude and Ω is Earth’s rotational constant. Although the DJF mean zonal wind does not truly characterize the flow on any given day, it is still a qualitatively useful diagnostic to understand and to compare the anticipated behavior of stationary Rossby waves in the GCMs. In linear dynamics, Rossby waves of stationary wavenumber k are anticipated to be reflected at or decay beyond the turning latitude in which $K_s = k$. Furthermore, Rossby waves are refracted toward values where $K_s > k$, so that regions where K_s is maximized, such as the westerly jets, act as waveguides (Hoskins and Ambrizzi 1993). Such general behaviors suggested by Rossby wave theory are useful indicators of how the basic state in the GCMs impacts Rossby wave propagation.

Figure 3 shows K_s as calculated by (1) for the six good MJO GCMs and ERA-Interim. Regions where the mean zonal wind is easterly ($\bar{u}_M < 0$) are in white. Based on Rossby wave theory, these are regions where Rossby waves cannot propagate. Areas where $\beta_M < 0$ are shaded in black. These regions indicate that the meridional gradient of absolute vorticity is reversed, and stationary Rossby waves must turn before these latitudes (e.g., Hoskins and Ambrizzi 1993). A reversal of the absolute vorticity gradient is often observed on the poleward flank of the subtropical jet, so that Rossby waves emitted by Indian Ocean or western Pacific heating must travel east before they can propagate north. In instances that the jet extends too far east (e.g., MRI-CGCM3 and GFDL CM3; Fig. 2), the region in which $\beta_M < 0$ also extends farther east (Fig. 3). Based on this simple quantity it is expected that in the models with an extended jet the MJO Rossby waves would travel farther east in the Pacific relative to reanalysis, leading to inaccuracies in the teleconnection patterns downstream.

MJO Rossby waves in the extratropics are generally characterized by stationary zonal wavenumber 2–4 (e.g., Seo et al. 2016). Since Rossby waves do not propagate

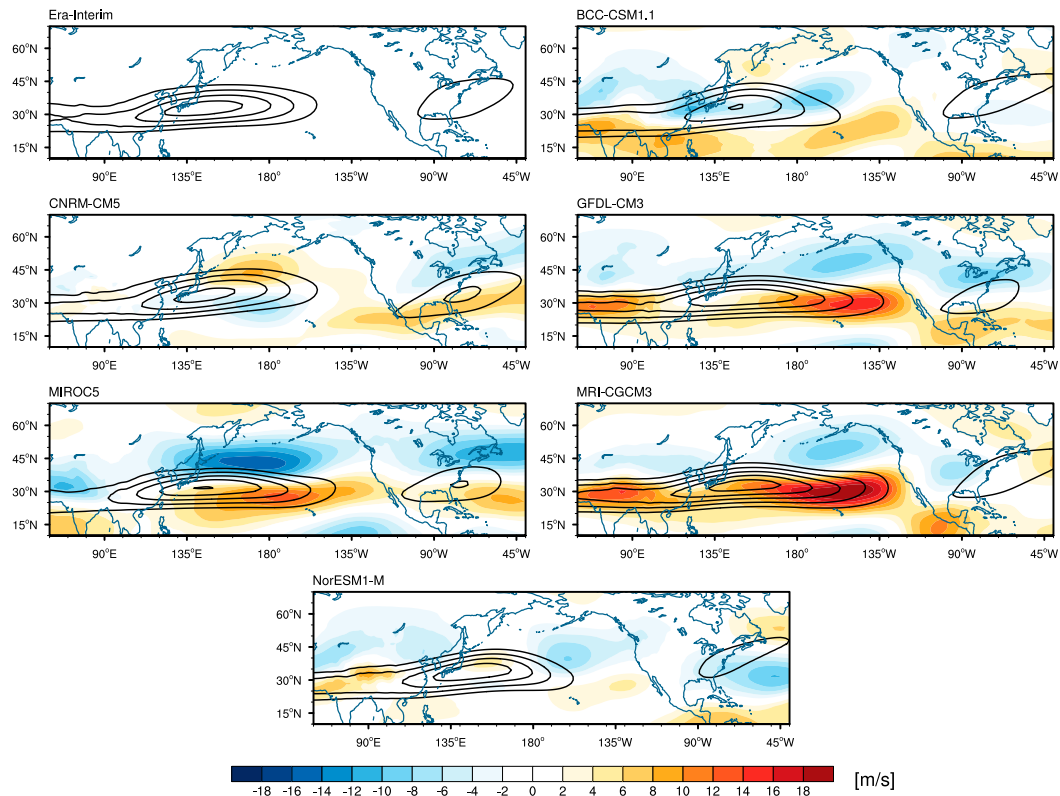


FIG. 2. Mean 250-hPa zonal wind (contours) for (top left) reanalysis and the good MJO models during DJF. Contours are every 10 m s^{-1} beginning at 35 m s^{-1} . Color shading represents the deviation of the model mean zonal wind from that of reanalysis.

beyond their corresponding turning latitude, an approximate boundary for MJO Rossby waves is the $K_s = 3$ contour. In ERA-Interim, BCC_CSM1.1, CNRM-CM5, and NorESM1-M, a $K_s = 2-4$ Rossby wave initiated by a Rossby wave source (RWS) in the Pacific subtropical jet will propagate east in the subtropical jet waveguide and may travel northeast over North America, following a waveguide bounded by the $K_s = 3$ contour. The GCMs with this northeast waveguide do not have a zonally extended subtropical jet. Similar Rossby waves may behave differently in GFDL CM3, MIROC5, and MRI-CGCM3, owing to the eastward extension of the $\beta_M < 0$ region. Figure 3 suggests that Rossby waves in these GCMs may propagate in a more zonally oriented pathway over the North Pacific.

c. MJO teleconnections

With a basic understanding of model MJO quality and the differences in the background flow, this section examines the MJO teleconnection patterns in the GCMs. The composite pentad 250-hPa geopotential height anomaly and anomalous tropical precipitation is examined for all 10 GCMs for each MJO phase. We define a pentad as the average from lag 0 to lag 4 of an MJO phase,

where lag 0 is the full unlagged MJO phase composite, lag 1 is the phase composite shifted by 1 day, and so on. In this definition, lag 0 is the composite of all DJF days in a given MJO phase where the RMM amplitude is greater than 1, including days in the same MJO event as well as all other strong events. The lagged pentad contains the average during that phase as well as out to four days after that MJO phase so that much of the Pacific teleconnection pattern associated with an MJO phase can be represented in one figure. A two-tailed Student's t test is used to determine the geopotential height anomalies found to be significantly different from zero using N/d_M independent samples, where N represents the number of days per MJO phase and d_M is the average length of an MJO phase ($d_M = 5$ for reanalysis; e.g., Henderson et al. 2016; Alaka and Maloney 2012). Values of N are provided in Table 3 in parentheses for each good MJO model and the model d_M values vary from 4 to 6.

The teleconnection patterns associated with MJO phase 3 (Fig. 4) and phase 7 (Fig. 5) are provided for the good MJO models as examples, along with composite MJO precipitation anomalies. These MJO phases, characterized by opposite-signed precipitation anomalies to each other, are chosen since their teleconnection patterns

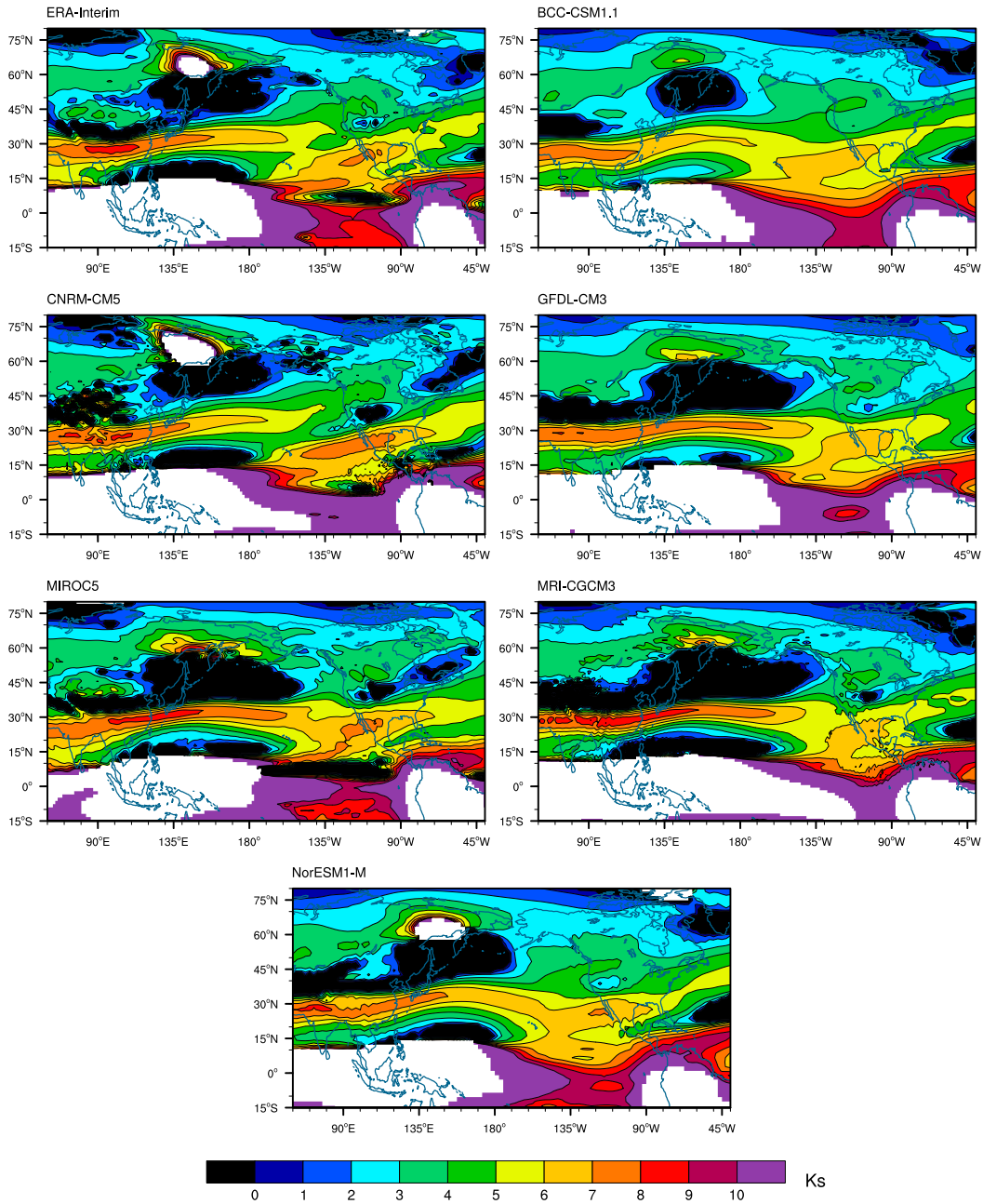


FIG. 3. Stationary zonal wavenumber (K_s) derived from the 250-hPa Mercator zonal wind during DJF. Areas of easterly winds ($\bar{u}_M < 0$) are in white, and regions where $\beta_M < 0$ are in black.

are associated with significant changes in much of the extratropical atmosphere (e.g., Lin et al. 2010), including robust changes in the NAO pattern and east Pacific and Atlantic blocking (e.g., Cassou 2008; Lin et al. 2009; Henderson et al. 2016). While all of the GCMs shown in Figs. 4 and 5 have a relatively good MJO, it is clear that the MJO teleconnection patterns have many differences from reanalysis (top left) in most cases. This is not surprising considering the large differences between the

model basic states previously discussed. In agreement with the discussion of Fig. 3, for example, the GCMs with an extended jet demonstrate an eastward shift in the MJO teleconnection patterns (e.g., MRI-CGCM3 and GFDL CM3). The MRI-CGCM3 and GFDL CM3 geopotential height anomalies east of the date line are significantly different from reanalysis at the 95% level based on a two-tailed difference of means test (not shown). Furthermore, the MIROC5 teleconnection patterns hint of a zonally

TABLE 3. Geopotential height anomaly pattern correlation coefficients between the good MJO models and reanalysis for each MJO phase calculated over the Pacific–North American region (15°N–80°N, 130°E–60°W). In parentheses is the number of days in each MJO phase (N).

Model	Phase 1	Phase 2	Phase 3	Phase 4	Phase 5	Phase 6	Phase 7	Phase 8
BCC_CSM1.1	0.53 (292)	0.29 (332)	0.64 (376)	0.74 (414)	0.41 (259)	0.36 (289)	0.73 (418)	0.55 (405)
CNRM-CM5	0.51 (361)	0.56 (438)	0.87 (566)	0.82 (386)	0.62 (359)	0.62 (349)	0.76 (594)	0.71 (360)
GFDL CM3	0.39 (340)	0.52 (347)	0.62 (492)	0.80 (380)	0.25 (263)	−0.01 (387)	0.39 (412)	0.82 (451)
MIROC5	0.55 (337)	0.72 (440)	0.67 (502)	0.48 (322)	0.45 (359)	0.40 (440)	0.73 (539)	0.89 (400)
MRI-CGCM3	0.73 (284)	0.71 (366)	0.28 (543)	0.55 (385)	0.17 (304)	0.10 (342)	0.22 (573)	0.71 (511)
NorESM1-M	0.14 (343)	0.62 (429)	0.66 (389)	0.48 (304)	−0.12 (321)	0.43 (447)	0.69 (419)	0.88 (365)

oriented pathway over the Pacific and North America, although the impact of such a pathway is unclear. A difference of means test suggests that regional east Pacific anomalies of the opposite sign as reanalysis in MIROC5 (Fig. 4) are significantly different from reanalysis at the 95% level (not shown). In addition to the basic state, the teleconnection patterns may be influenced by errors in the amplitude and structure of MJO precipitation anomalies (color shading). In the bad MJO models (not shown), the teleconnection patterns tend to either show no resemblance to reanalysis or be very weak.

To better quantify the differences in the teleconnection patterns between the models and reanalysis, pattern correlations of 250-hPa geopotential height anomalies between reanalysis and each model are calculated for all MJO phases over the Pacific and North American region (15°N–80°N, 130°E–60°W). These values are provided for each MJO phase of the good MJO models in Table 3. The teleconnection pattern correlations are then averaged over all MJO phases for each model and represented in Fig. 6 (y axis in both panels). CNRM-CM5 has the highest average teleconnection pattern correlation and GFDL-ESM2G the lowest. Not surprisingly, the poor MJO models have relatively low average pattern correlations. Some of the good MJO models, however, tend to produce as poor of teleconnection patterns as the poor MJO models, such as GFDL CM3, NorESM1-M, and MRI-CGCM3. To begin to understand why this may be the case, the teleconnection pattern correlations are first compared to the E/W ratio MJO skill metric previously calculated (Fig. 6a, x axis). Comparison to the E/W ratio shows that the models with a relatively good MJO tend to have better MJO teleconnection patterns, with a correlation of 0.61 between the axes (excluding the ERA-Interim reference correlation), which is significant at the 90% confidence bounds based on a two-tailed test. However, a good MJO does not necessarily mean accurate representation of the MJO teleconnection patterns. For example, MRI-CGCM3 has an average teleconnection pattern correlation of only 0.43, despite having the closest MJO E/W ratio to observations. This suggests that to better understand the skill of the MJO teleconnection

patterns, it is important to examine the basic state as well as the structure of anomalous MJO convection.

The teleconnection pattern correlations are compared to two basic state skill metrics derived from the DJF mean 250-hPa zonal wind U_{250} . The first basic state skill metric for the good MJO models is the root-mean-square (RMS) error of U_{250} over the Pacific domain (15°–60°N, 110°E–120°W; Fig. 6b, plus symbols). The highest U_{250} RMS errors are observed in MRI-CGCM3 and MIROC5. The former has the largest eastward extension of the jet out of all the models, whereas the latter exhibits the southward shift of the Pacific jet (Fig. 2). However, MIROC5 has the second highest average teleconnection pattern correlation, indicating that teleconnection pattern error is not likely related with overall error in zonal wind. In fact, the U_{250} error for the full Pacific domain is poorly correlated with MJO teleconnection skill ($r = -0.31$).

The second U_{250} skill metric specifically focuses on the longitudinal errors of the subtropical jet. This metric is calculated by finding the latitude of the maximum winds in the subtropical jet for both models and reanalysis, isolating latitudes 5° to the north and to the south of this maximum, and then calculating the RMS error between the model and ERA-Interim DJF mean U_{250} within the region defined by these latitudes and longitudes 110°E–120°W. This ensures that the RMS error is based on the longitudinal error of the jet, and not any latitudinal shifts. The longitudinal RMS error skill metric (Fig. 6b, filled circles) has a correlation of -0.64 with the teleconnection pattern correlations (y axis). In general, the models with an eastward-extended jet tend to have lower average teleconnection pattern skill among the good MJO models. The exception is NorESM1-M, which has a similar zonal wind RMS error as CNRM-CM5. Although its pattern correlation during phase 3 is relatively good ($r = 0.66$; Table 3), its lower average teleconnection pattern correlation may be due to the structure of the model MJO precipitation anomalies, which tends to be zonally elongated (e.g., Figs. 4 and 5) during most MJO phases.

The combined impact of the basic state subtropical jet and MJO quality on the MJO teleconnection patterns, as well as some differences in teleconnection skill during

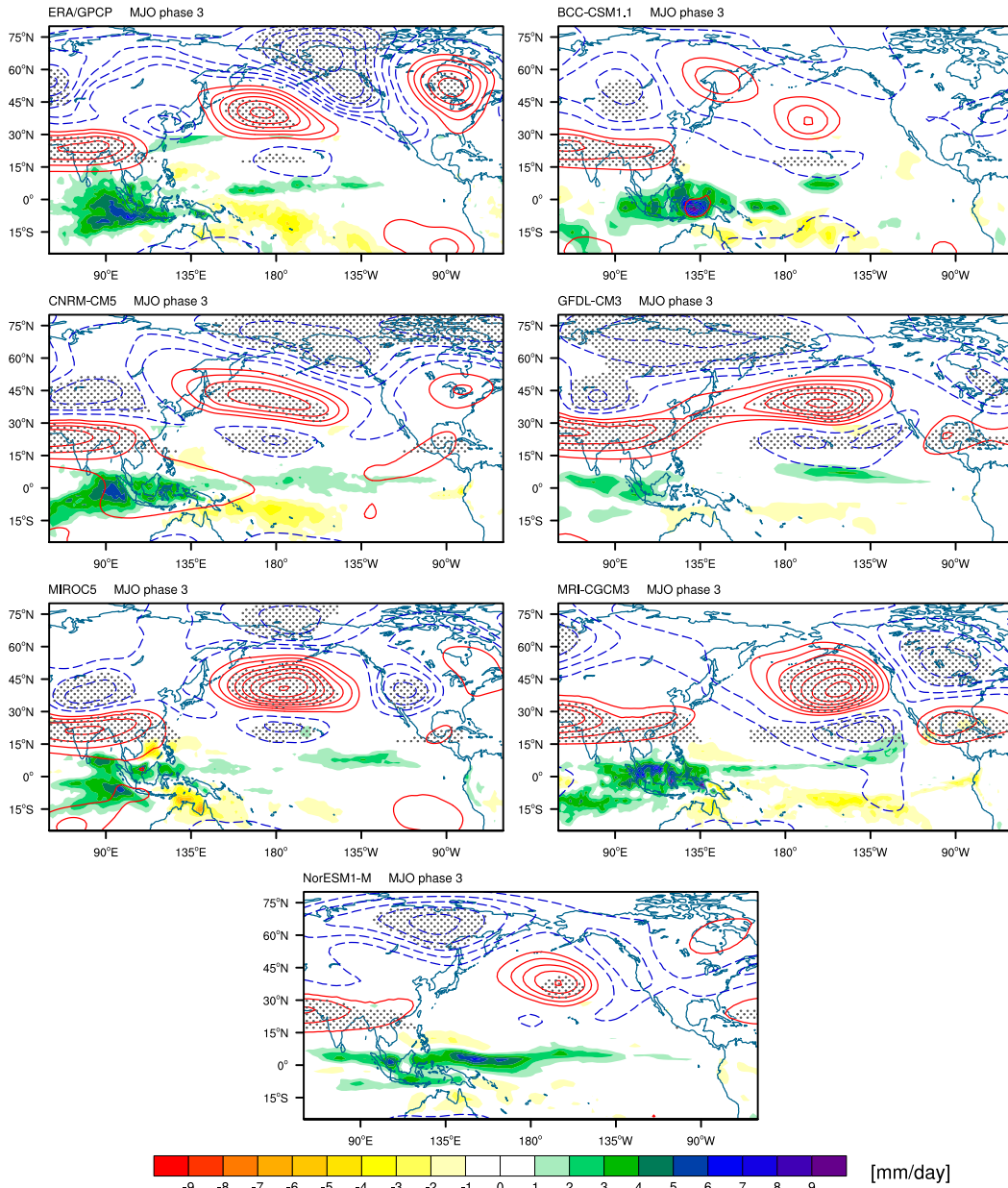


FIG. 4. MJO phase 3 pentad composites of anomalous 250-hPa geopotential height, where a pentad denotes a 5-lag mean, or the field average of lags 0–4 following an MJO phase. Positive geopotential height anomalies are in red solid contours, and negative anomalies are in blue dashed contours. Contours are every 10 m, and the zero contour is omitted. Anomalies found to be 95% significantly different from zero are dotted. The color shading shows the anomalous tropical precipitation composite during MJO phase 3.

different MJO phases, can be better understood by examining the RWS associated with each MJO phase. Following [Sardeshmukh and Hoskins \(1988\)](#), the RWS can be defined as follows:

$$RWS = -\nabla \cdot (\mathbf{V}_\chi \zeta) = -\mathbf{V}_\chi \cdot \nabla \zeta - \zeta D, \quad (3)$$

where ζ is the absolute vorticity, \mathbf{V}_χ is the irrotational (divergent) component of the horizontal wind vector,

and $D = \nabla \cdot \mathbf{V}_\chi$. The right-hand side of (3) demonstrates that the RWS can be described as the sum of the advection of absolute vorticity and vortex stretching by the divergent wind. The signs of RWS anomalies are relative to the background absolute vorticity, with positive RWS in regions of divergence (convergence) in downgradient (upgradient) mean absolute vorticity (e.g., [Hsu 1996](#)). The anomalous RWS at 250 hPa

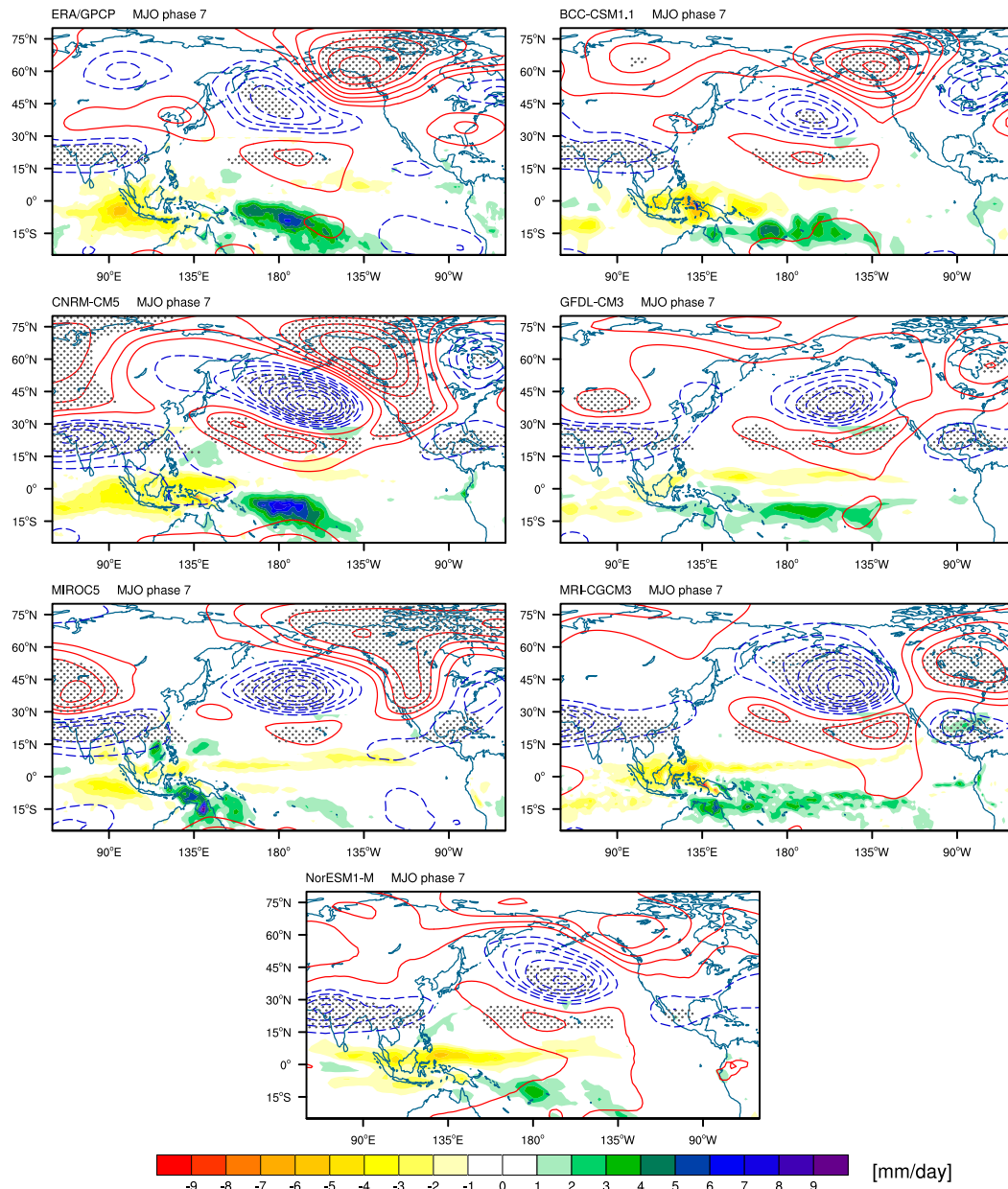


FIG. 5. As in Fig. 4, but for MJO phase 7.

composited relative to MJO phase 3 is shown in Fig. 7 for the good MJO models. For reference, the $K_s = 3$ contour is overlaid and the $\beta_M < 0$ region is hatched (see Fig. 3). Although only phase 3 is shown as an example, anomalous RWS characteristics are very similar for all MJO phases for most models.

Examining the two terms of (3) independently (not shown) indicates that for most of the models, the RWS anomalies during most MJO phases (including phase 3) are largely due to vortex stretching by the divergent wind. The anomalous divergence field associated with

MJO convection leads to anomalous convergence generally on the southern flank of the subtropical Pacific jet that generates anomalous vorticity and triggers Rossby waves such as those shown in Figs. 4 and 5. This process is the primary component of the RWS in all models during MJO phase 3 except in MRI-CGCM3, which has a stronger contribution from the advection of absolute vorticity that is overestimated relative to reanalysis. As a result, MRI-CGCM3 has a strong anomalous RWS east of the strongest RWS anomaly in ERA-Interim (Fig. 7).

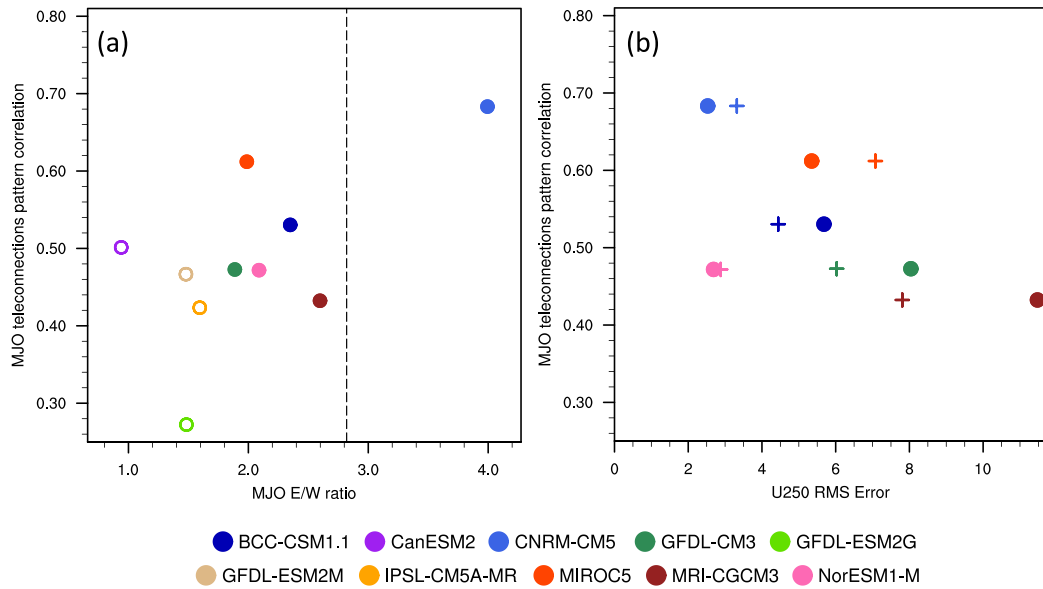


FIG. 6. Teleconnection pattern correlation averaged for all MJO phases (y axes) relative to the (a) MJO E/W ratio and (b) the 250-hPa mean zonal wind RMS error. In (a), the dashed line indicates the observed E/W ratio, and the open circles represent the poor MJO models. In (b), the plus signs show the model zonal wind RMS error over the full Pacific basin, while the filled circles indicate the longitudinal RMS error in the region of the subtropical jet. See text for more detailed explanations.

For MJO phases 2–3 (only phase 3 shown; Fig. 7), BCC_CSM1.1 and NorESM2-M produce weaker anomalous RWS than reanalysis and typically the weakest RWS relative to all of the good MJO models examined here. However, both models demonstrate a stronger RWS anomaly during MJO phases 6–7 (not shown) that are more comparable to reanalysis. This difference in RWS strength may partially explain the weaker MJO teleconnection patterns during MJO phase 3 (Fig. 4) relative to phase 7 (Fig. 5) in the two models.

Of particular interest is the anomalous RWS of the opposite sign east of the date line that is prominent in some models and ERA-Interim, although the longitudinal position of this anomaly varies (Fig. 7). For example, there is a strong positive RWS anomaly near 135°W that extends over the western coast of North America in MRI-CGCM3 and GFDL CM3, whereas the positive RWS is near 150°W in ERA-Interim. The positive anomalous RWS, caused by anomalous convergence, coincides with the exit region of the jet, as evident when comparing the RWS anomaly to the extent of the jet (cf. Figs. 2 and 7), and likely affects the teleconnection patterns across the Pacific and North America. In other words, the erroneous eastward shift of the positive RWS anomaly may partially account for some of the differences observed in the MRI-CGCM3 and GFDL CM3 teleconnection patterns relative to other models and ERA-Interim (Figs. 4 and 5).

4. LBM experiments

One issue with the composite analysis above is that it is not easy to separate the impact of model MJO convection from the influence of the model basic state for determining the quality of the teleconnection pattern. We therefore employ an LBM in this section to examine the impact of the model MJO and basic state independently in order to better understand the differences in the teleconnection patterns.

a. LBM description and setup

In the LBM, the hydrostatic primitive equations on a sphere are linearized about a basic state and the linear response to a prescribed forcing is calculated (Watanabe and Kimoto 2000). The resolution is set to T42 with 20 sigma levels in the vertical. For the numerical damping, horizontal diffusion with an e -folding time scale of 2 h for the largest wavenumbers is set. The model also employs Newtonian damping with a time scale of 20 day⁻¹ for most vertical levels and a time scale of 0.5 day⁻¹ for the lowest and highest levels. These parameters are set to be the same for all experiments to ensure that the differences in the LBM results are due to differences in MJO heating and the basic state, not due to changes in the LBM parameters. For more specific details on the LBM beyond that described here, please refer to Watanabe and Kimoto (2000).

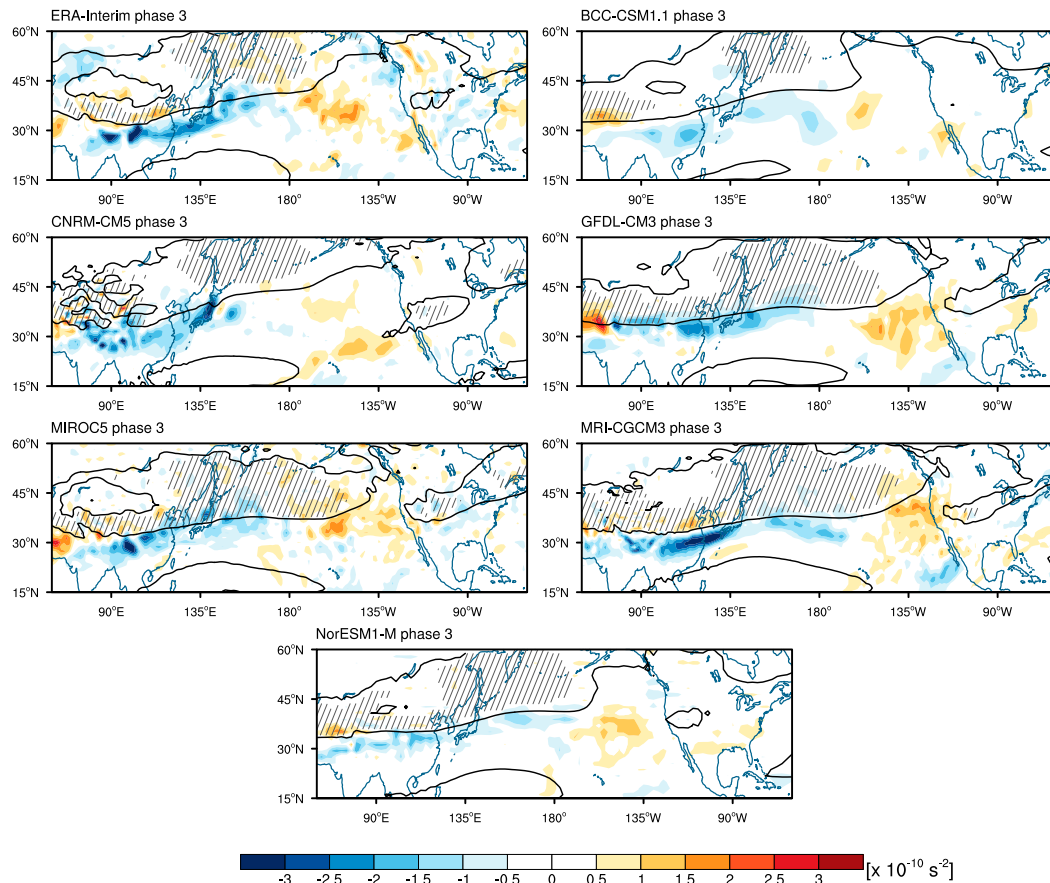


FIG. 7. Pentad anomalous Rossby wave source (RWS; color shading) composited relative to MJO phase 3 for (top left) reanalysis and the good MJO models. For reference, the $K_s = 3$ contour line from Fig. 3 is overlaid, and the $\beta_M < 0$ regions north of 25°N are hatched.

The anomalous MJO apparent heat source Q_1 of each GCM is used to force the LBM. Formulated by Yanai et al. (1973), Q_1 includes heating associated with radiation, latent heat release due to phase changes of water, and the vertical eddy transport of sensible heat. The three-dimensional Q_1 is derived as a residual from the dry static energy s budget, where $s = c_p T + gz$, T is the temperature, c_p is the specific heat capacity of air at a constant pressure, g is the gravitational constant, and z is the height. The heat source Q_1 is represented by

$$Q_1 = \frac{\partial s}{\partial t} + \nabla \cdot (s\mathbf{V}) + \frac{\partial(s\omega)}{\partial p}, \quad (4)$$

where \mathbf{V} is the horizontal wind vector and ω represents the pressure velocity. The anomalous heat source is calculated as follows: First, Q_1 anomalies Q'_1 are computed by removing the long-term daily mean and first three harmonics of the seasonal cycle from Q_1 [(4)]. Second, Q'_1 is composited relative to MJO phase for ERA-Interim and each GCM, resulting in eight MJO

phase latitude–longitude Q'_1 composite maps. Third, in order to capture the eastward propagation of the MJO, Q'_1 is linearly interpolated in time between adjacent MJO phases. Each MJO phase is assumed to last 6 days. This length is idealized since the length of an MJO phase will vary from model to model as well as from phase to phase within a model (e.g., Fig. 1). The average length of MJO phases 3 and 7 between all of the good MJO models and reanalysis is calculated to be 6 days, so this value is chosen. The final propagating heat source for each dataset is then a series of Q'_1 composite maps over the course of a 48-day idealized MJO cycle beginning at MJO phase 1.

In the experiments described below, the model is forced with the propagating Q'_1 as described above, and the model response is shown as the average 250-hPa geopotential height anomaly from days 8–18, which corresponds to the latter half of phase 2 and all of phase 3. Similar results were obtained with a stationary phase-2 forcing used to spin up the LBM for 3 to 5 days prior to propagating the MJO heat source eastward (not shown).

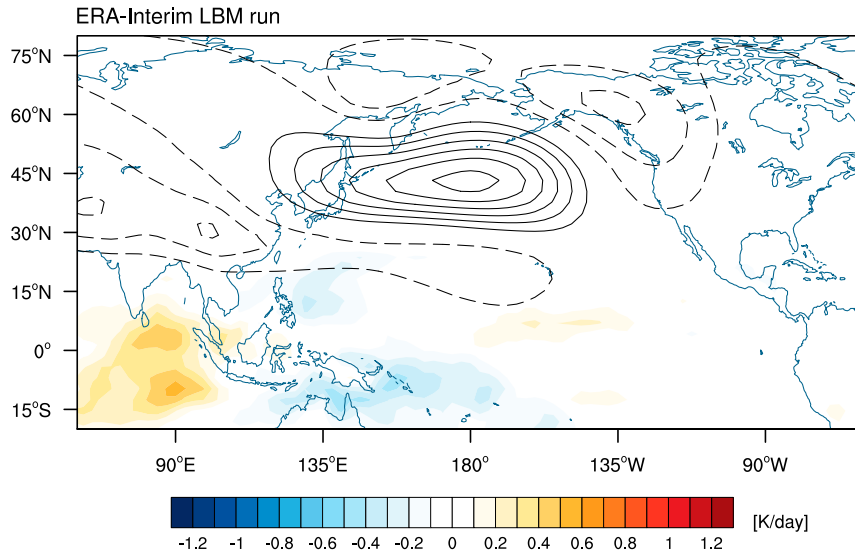


FIG. 8. Anomalous 250-hPa geopotential height response (contours) to the reanalysis Q_1 against the reanalysis basic state. Shown is the average 8–18-day response to a propagating heat source initiated during MJO phase 1 and coinciding with MJO phases 2–3. See text for further details regarding the propagating heat source used. Contours are every 5 m and the zero contour is omitted. The color shading shows the 1000- to 200-hPa 8–18-day averaged reanalysis Q_1 .

A propagating MJO heat source (e.g., Matthews et al. 2004) is used here instead of a steady single-phase heat source (e.g., Seo and Son 2012) because MJO phase 2 also likely plays an important role in the teleconnection patterns shown in Fig. 4. This is a reasonable assumption given the decay time scales of MJO phases (e.g., Fig. 1), which for the good MJO models tend to persist the MJO for more than one phase. The time it takes Rossby wave propagation to reach the North Pacific and North America from the tropical warm pool also typically exceeds one MJO phase (e.g., Lin et al. 2009). Because of the use of a propagating heat source, the LBM does not reach steady state. We note that the time period of the response is chosen to highlight the teleconnection pattern over the Pacific basin; anomalies over North America associated with the MJO may not yet have fully developed to allow a direct comparison to Fig. 4.

b. LBM basic state and MJO heating experiments

Three sets of experiments are carried out for each good MJO model in addition to a reference run using reanalysis. First, both the GCM basic state and the GCM Q_1 are used to assess the ability of the LBM to reproduce the Pacific MJO teleconnection patterns shown in Fig. 4 (hereby referred to as the Q1BS runs). To determine the impact of the GCM basic states for producing model bias in the teleconnection patterns, the LBM is then run using the reanalysis Q_1 with the basic state of each GCM (hereby referenced as the BS runs).

The influence of the GCM's MJO heating is then examined by using the GCM Q_1 in conjunction with the reanalysis basic state (referred to as the Q1 runs).

The geopotential height response for the reference run, which utilizes the reanalysis Q_1 with the reanalysis basic state, is shown in Fig. 8. The reference run reasonably captures the general location of the Pacific anomalies relative to reanalysis (Fig. 4) with a pattern correlation of 0.72 for the region 15°–80°N, 120°E–120°W. Also shown are the LBM experiments for MRI-CGCM3 (Fig. 9), CNRM-CM5 (Fig. 10), and MIROC5 (Fig. 11). For brevity, the LBM runs associated with the other good MJO models are discussed as appropriate but not shown. (The statistics from these other simulations will be compiled below in Fig. 13, however.)

c. LBM runs with model BS and Q_1

The geopotential height response of the Q1BS runs is shown in the third panel of Figs. 9–11 (black contours) for the three GCMs previously mentioned. Also shown in color contours is the difference between the average Q1BS geopotential height response and the average from the reference run (Fig. 8). To determine how well the LBM captures the Pacific teleconnection pattern associated with the early phases of the MJO, and therefore justifying the use of the LBM, pattern correlations for the geopotential height anomalies are calculated for 15°–80°N, 120°E–120°W between the Q1BS runs for all good MJO models (e.g., third panels

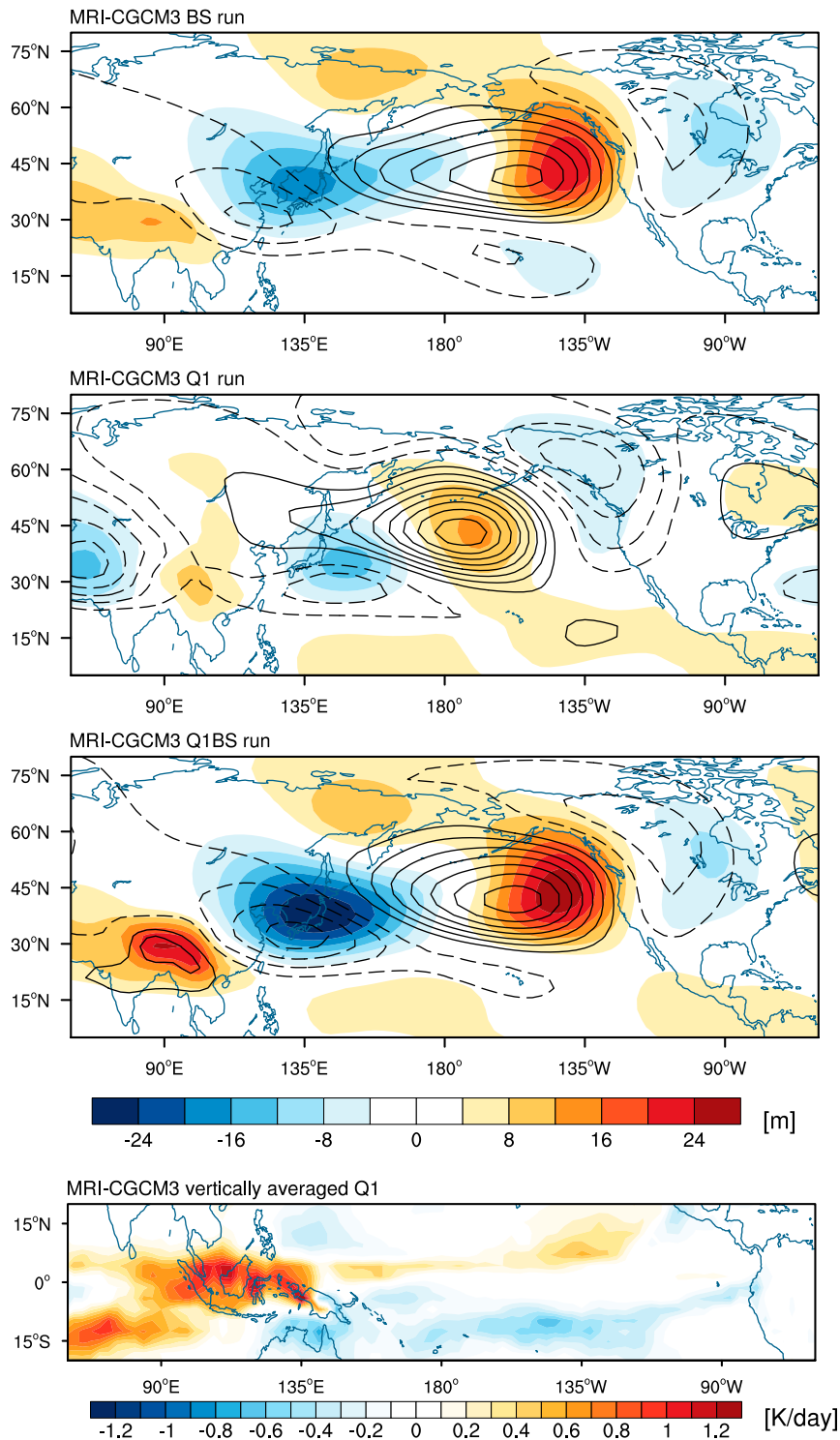


FIG. 9. Anomalous 250-hPa geopotential height 8–18-day average LBM response (contours) to (from top to bottom) reanalysis Q_1' against the MRI-CGCM3 basic state (referred to as the MRI-CGCM3 BS run), MRI-CGCM3 Q_1' against the reanalysis basic state (MRI-CGCM3 Q1 run), and MRI-CGCM3 Q_1' against the MRI-CGCM3 basic state (MRI-CGCM3 Q1BS run). Contours are every 5 m and the zero contour is omitted. Color shading is the difference between each MRI-CGCM3 LBM run and the reference run shown in Fig. 8. (bottom) The 8–18-day average MRI-CGCM3 Q_1' .

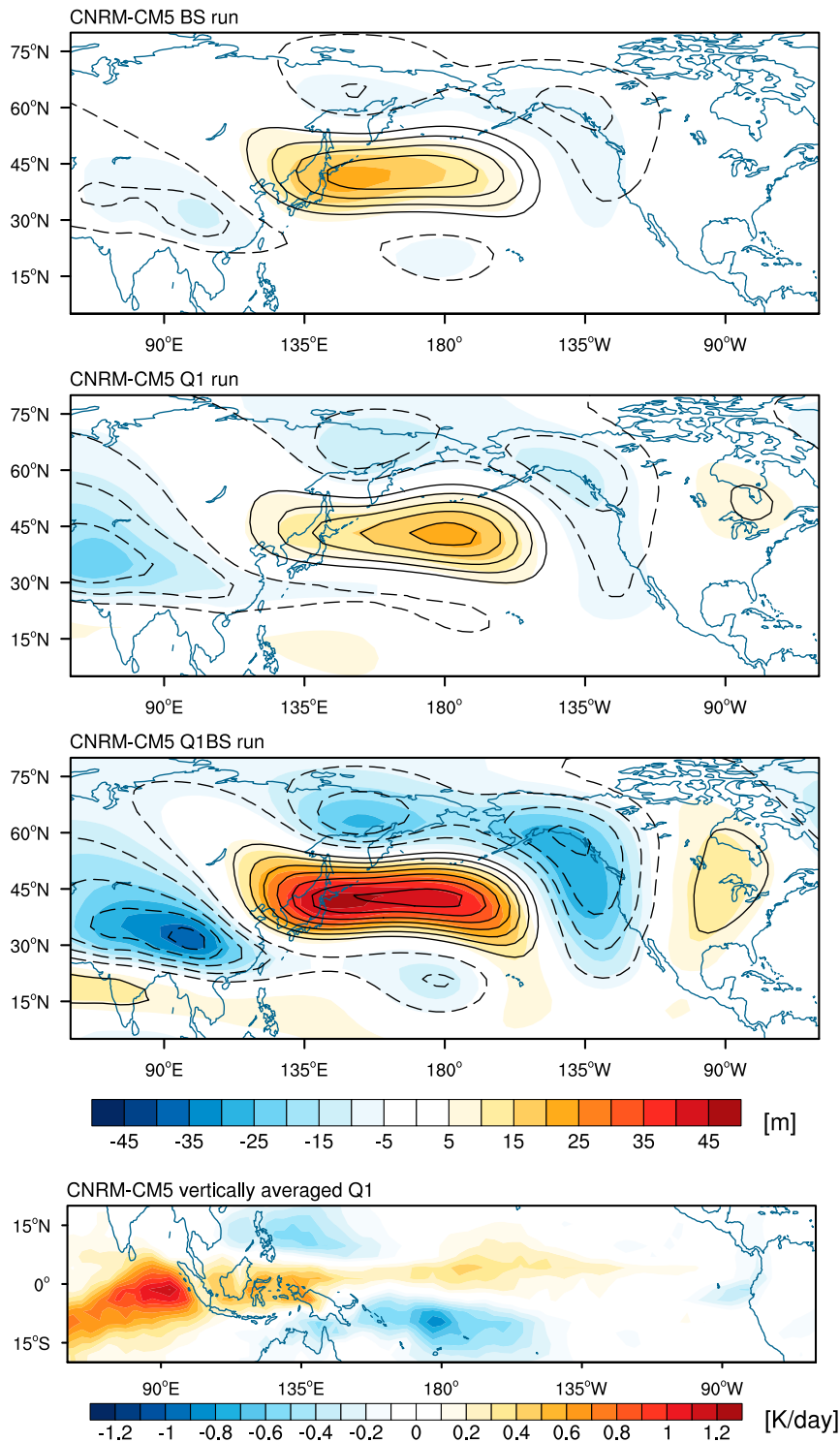


FIG. 10. As in Fig. 9, but for CNRM-CM5. Because of a stronger LBM response, the geopotential height anomaly contour interval is increased to 10 m.

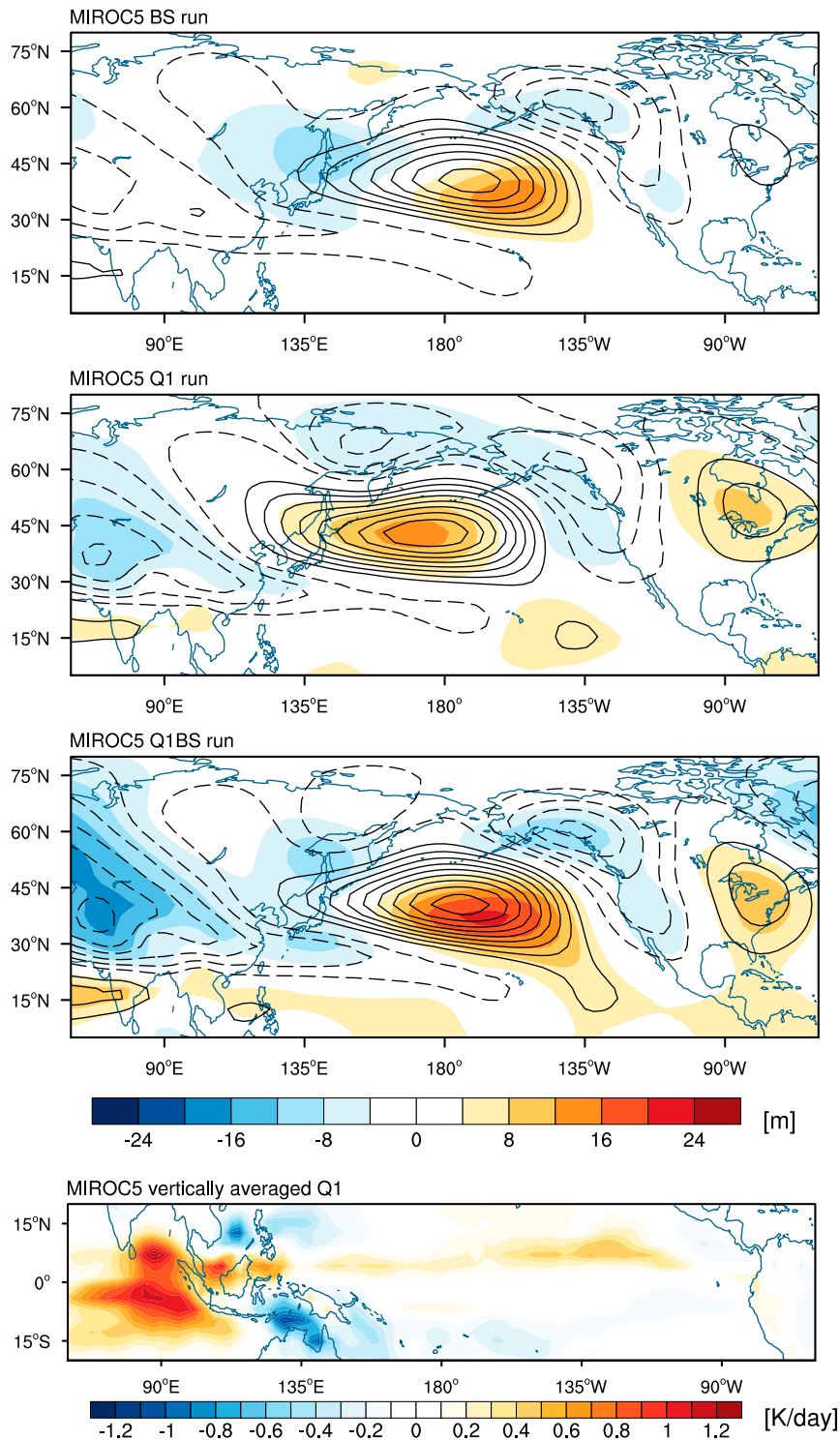


FIG. 11. As in Fig. 9, but for MIROC5.

of Figs. 9–11, black contours) and their corresponding composites from Fig. 4. The average pattern correlation is 0.79, with individual pattern correlations ranging from 0.66 to 0.91. These pattern correlations exclude

North America, which is not yet fully developed in many of the LBM experiments shown.

The Q1BS runs demonstrate that the LBM is able to capture some of the teleconnection pattern biases in

Fig. 4. For example, the MRI-CGCM3 Q1BS run shows a clear eastward shift of the anticyclonic anomaly over the Pacific relative to ERA-Interim, as highlighted by the color contours (Fig. 9, third panel). There also appears to be a portion of the response in the Q1BS runs for the MIROC5 run (Fig. 11) that is more zonally oriented, indicated by a southward extension of the negative geopotential height anomaly over western North America (see color shading) relative to the reanalysis reference run (Fig. 8). A possible cause of this southward extension will be discussed in section 4d but was also suggested by Fig. 3. In addition, clear differences exist in the amplitude of the responses. This is particularly true for the CNRM-CM5 Q1BS run (Fig. 10, third panel), which has a very similar pattern to the reference run but has geopotential height anomaly differences of up to 45 m (color contours). This amplitude difference may be an artifact of using the same LBM parameters such as damping coefficients for all LBM runs and will be discussed in more detail at the end of this section (section 4f).

d. Basic state and Q1 runs

In agreement with the basic state discussion (section 3b), the GCMs containing an eastward-extended Pacific subtropical jet result in an eastward shift of the teleconnection patterns (e.g., Fig. 9, top panel) relative to the reanalysis reference run (Fig. 8). The MRI-CGCM3 BS run, which has the greatest jet extension of the model basic states, demonstrates the largest eastward shift in the anticyclonic Pacific anomaly out of all of the LBM BS runs. An eastward shift is also evident in the GFDL CM3 BS run (not shown) as well as, to a lesser extent, the MIROC5 BS run (Fig. 11). The extended Pacific jet has downstream effects on the teleconnection pattern. For example, the negative geopotential height anomaly over Alaska and the Pacific Northwest in the reference run (Fig. 8) develops farther eastward in MRI-CGCM3 (Fig. 9, top panel). Anomalies over northeast North America and the Atlantic also contain errors associated with this shift at later times (not shown).

Some evidence exists for a more zonally oriented pathway in the BS runs of the models with an extended jet, in agreement with the discussion in section 3b. For example, the negative geopotential height anomaly center over North America in the MRI-CGCM3 BS run (Fig. 9, top) is shifted south relative to the same anomaly in the reference reanalysis run (Fig. 8). The behavior is also seen in the other runs with an extended jet [e.g., MIROC5 (Fig. 11) and GFDL CM3 (not shown)]. This suggests that errors in a GCM's basic state can shift the direction of Rossby wave propagation as previously discussed in reference to Fig. 3.

The importance of the GCM MJO heating perturbations to the quality of the teleconnection patterns is

investigated by forcing the LBM with each GCM's Q'_1 but using the reanalysis basic state (Figs. 9–11, second panels). Although the structure of Q'_1 varies greatly from one GCM to the other (Figs. 9–11, bottom panels), the circulation anomalies from the Q1 runs appear qualitatively similar to the reference run (Fig. 8), with the most apparent difference being in the amplitude of the response. For example, the NorESM2-M Q'_1 field (not shown), which has comparable amplitude to the reanalysis Q'_1 (Fig. 8), is zonally elongated with an Indian Ocean heating that is split about the equator (e.g., Fig. 4, precipitation field). Despite the large differences from the reanalysis Q'_1 , forcing the LBM with this heating produces a teleconnection pattern similar to reanalysis with the key difference being the amplitude of the response (not shown). As discussed in Sardeshmukh and Hoskins (1988) and references therein, the model response to tropical heating near the subtropical jet is relatively insensitive to the longitudinal location of the heating. Referring back to the RWS associated with each GCM (Fig. 7), it can be seen that despite the differences in Indo-Pacific Q'_1 structure and location, the RWS still maximizes in the subtropical jet where it can efficiently generate Rossby waves.

Some of the errors in the GCM teleconnection patterns (Fig. 4) may be due to the Q'_1 east of the date line (e.g., Figs. 9–11, bottom), which is associated with a RWS that occurs near the exit region of the subtropical jet (e.g., Fig. 7). The influence of this heat source was examined through a sensitivity test using the basic state and Q'_1 of MRI-CGCM3, except that Q'_1 is set to zero east of 170°W, thereby eliminating the heat source east of the date line. The average 8–18-day geopotential height anomaly response (Fig. 12, top panel) shows an overall weakening in amplitude, with the exception of the anomalous anticyclone north of the western Indian Ocean, which is slightly strengthened. Furthermore, the negative geopotential height anomaly over North America is shifted north relative to the Q1BS run shown in Fig. 9. This northward position better aligns with the negative geopotential height anomaly in the reference run (Fig. 8). This anomaly, however, is still shifted east relative to the reference run due to the MRI-CGCM3 basic state. These results suggest that MJO heating east of the date line influences the amplitude and pathway of MJO Rossby waves. Similar results were obtained with MIROC5 (Fig. 12, bottom panel) and CNRM-CM5 (not shown) when setting Q'_1 to zero east of 170°W and east of the date line, respectively. In the MIROC5 modified experiment (Fig. 12, bottom panel), the zonally oriented pathway present in the Q1BS run (Fig. 11, third panel) was largely reduced. This suggests that in addition to the errors introduced by the basic state, the Q'_1 east of the date

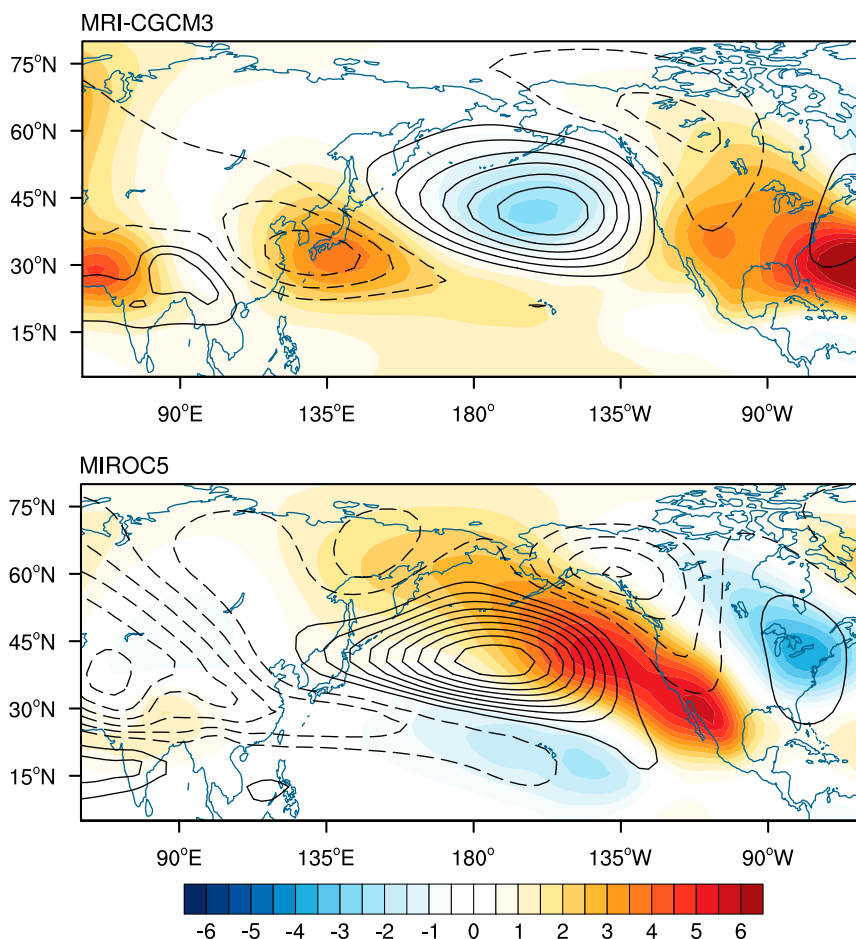


FIG. 12. Anomalous 250-hPa geopotential height 8–18-day average LBM response (contours) to (top) a modified MRI-CGCM3 Q_1' against the MRI-CGCM3 basic state and (bottom) a modified MIROC5 Q_1' against the MIROC5 basic state. LBM runs are modified by setting Q_1' to zero east of 170°W. Contours are every 5 m and the zero contour is omitted. Color shading represents the difference between each corresponding GCM Q1BS run and the modified Q_1' run.

line may contribute to the zonally oriented teleconnections previously mentioned for the LBM experiments and the teleconnection pattern composites (Figs. 4 and 5). We note, however, that more work is needed to understand the impact of the zonally oriented teleconnections.

A caveat is that the LBM does not allow interactions with the background flow nor nonlinear feedbacks; rather, it calculates the direct response to the MJO heating. Although this is an idealized assumption, the LBM can recreate many features of the composite teleconnection patterns of interest here, suggesting that the teleconnection patterns are primarily forced by MJO heating and not a result of internal extratropical variability.

e. LBM teleconnection pattern skill

To better quantify the improvement or degradation associated with the model MJO heating anomalies and/or

basic state to the teleconnection patterns in the LBM across all models, pattern correlations are calculated between the response of the LBM experiments and the ERA-Interim reference run for the Pacific region (120°E–120°W; Fig. 13). The BS runs (open circles) have a lower pattern correlation than the Q1 runs (squares) in the majority of models, with the largest differences for MRI-CGCM3. This suggests that in good MJO GCMs, large errors in the basic state may potentially degrade the teleconnection patterns more than errors in the Q_1' structure. An exception is NorESM1-M, which has a relatively good basic state (e.g., Fig. 2), so the impact of the Q_1' structure is more prominent. Similar LBM experiments were performed using a propagating heat source beginning in MJO phase 5, where the 8–18-day average approximately represents the middle of MJO phase 6 and all of MJO phase 7. Most of these LBM runs exhibit very similar characteristics as those

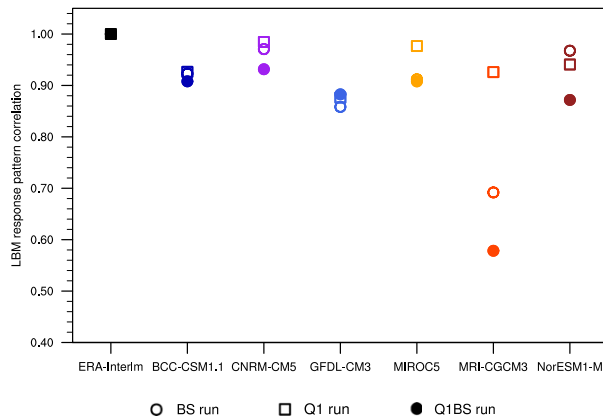


FIG. 13. Teleconnection pattern correlation between the LBM reference reanalysis run and each GCM LBM experiment for the 8–18-day average response initialized by MJO phase-1 heating. The averages approximately correspond to MJO phases 2–3. Correlation coefficients are provided for the BS runs (open circles), the Q1 runs (open squares), and the Q1BS runs (filled circles).

discussed for the MJO phase-2–3 LBM experiments, and hence these results are not shown here.

f. LBM response amplitude

As previously mentioned, a very noticeable difference between many of the GCM runs and the reference run is the amplitude of the circulation anomalies. One possibility for these variations in amplitude is differences in basic state tropical static stability, which modulates the strength of divergence associated with an MJO Q_1 anomaly (e.g., Maloney and Xie 2013). Environmental static stability can be represented by the time mean vertical gradient of dry static energy ($\partial\bar{s}/\partial p$). On characteristic time scales of the MJO, the dominant thermodynamic energy balance in the tropics that results from conditions of weak temperature gradients is the following (Wolding et al. 2016):

$$Q_1' = \omega' \frac{\partial\bar{s}}{\partial p}, \quad (5)$$

where ω' is the vertical velocity perturbation associated with the MJO convection. The DJF mean 200–500-hPa vertically averaged static stability is calculated for each good MJO GCM over the MJO region (60°E–180°, 20°S–20°N). The areal average for each model is provided in Table 2. All models, particularly CNRM-CM5 and MIROC5, underestimate the maximum amplitude of the environmental static stability. In the BS runs, where Q_1' remains the same for all models, a decrease in dry static stability amplitude would be balanced by a relative increase in ω' based on (5). Stronger ω' associated with MJO heating would scale with stronger upper-level divergence (e.g., Maloney and Xie 2013) and

thereby higher-amplitude stationary Rossby wave amplitudes such as that shown by the CNRM-CM5 BS run (Fig. 10, top panel). In the Q1 runs, where the dry static stability is determined by reanalysis, an increase in Q_1' amplitude can also lead to higher-amplitude anomalies relative to reanalysis. This can be seen in the CNRM-CM5 Q1 run (Fig. 10, second panel), which simulates a near doubling of the vertically averaged Q_1' amplitude in the west Indian Ocean (Fig. 10, bottom) relative to reanalysis. While an increase in Rossby wave amplitude is evident in the LBM runs, which assumes the same damping for all GCMs, Figs. 4 and 5 do not show similar amplitude differences. Errors in tropical static stability or Indo-Pacific Q_1' amplitude appear to have minimal influence on the amplitude of MJO Rossby waves, suggesting the GCMs themselves likely offset these errors with stronger damping of waves.

5. Summary and discussion

The MJO teleconnection patterns in 10 CMIP5 models are examined and compared. Composite analysis and the use of simple skill metrics demonstrated that some models with a relatively good MJO produce poor MJO teleconnections due to errors in the model basic state. The good MJO models with the lowest ability to recreate the MJO teleconnection patterns are those with a zonally extended Pacific subtropical jet (e.g., MRI-CGCM3 and GFDL CM3), which also show an eastward shift in the teleconnection patterns. Utilizing an LBM, the eastward shift in the teleconnection patterns was found to be primarily due to errors in the model basic state rather than MJO structure. Furthermore, MRI-CGCM3 and GFDL CM3, as well as MIROC5, which has a lesser jet extension than MRI-CGCM3 and GFDL CM3, suggest a zonally oriented Rossby waveguide in the mean state (Fig. 3). Rossby waves in these models may propagate along a zonal pathway (e.g., MIROC5; Fig. 4). These basic state errors can lead to teleconnection pattern errors downstream, suggesting that the model representation of the basic state, and especially the subtropical jet, must be considered when examining extratropical atmospheric phenomena that are strongly influenced by MJO activity.

In addition to the model basic state, MJO heating biases, even in models with a relatively good MJO, can lead to errors in the teleconnection patterns. LBM sensitivity experiments removing the GCM Q_1' east of 170°W resulted in a northward shift of the cyclonic anomaly over North America, indicating that Q_1' east of the date line can impact the extratropical MJO teleconnections. However, characteristics of Indo-Pacific heating in good MJO models appear to have relatively

little impact on the location of teleconnection patterns, in agreement with the arguments of Hoskins and Ambrizzi (1993) and others.

Some models tend to better reproduce the MJO teleconnection amplitude and pathway associated during some MJO phases relative to other phases. As previously discussed, BCC_CSM1.1 and NorESM1-M have weaker teleconnection patterns associated with MJO phase 3 (Fig. 4) than with phase 7 (Fig. 5). Furthermore, some GCMs better reproduce the teleconnection patterns associated with certain MJO phases relative to others (see Table 3). This suggests that a model may be able to reproduce the extratropical impacts associated with, for example, MJO phase 3 [e.g., suppressed east Pacific and Atlantic blocking (Henderson et al. 2016) or a positive NAO pattern (Lin et al. 2009)], but it may not be able to reproduce the opposite response and opposite impacts associated with MJO phase 7. This can lead to biases on longer time scales associated with those extratropical phenomena.

The results presented here demonstrate that both the model MJO and the basic state must be accurately represented in order to reproduce the MJO teleconnection patterns. However, as discussed in the introduction, improvements in MJO representation are often associated with a degradation of the basic state. This issue was highlighted in Yoo et al. (2015), who found that improving the model's convection scheme resulted in improved MJO simulation and MJO teleconnections in CAM5, without degrading the model basic state. Moving forward, more research such as that presented in Yoo et al. (2015) is needed to improve model MJO representation without degrading the associated MJO teleconnection patterns through basic state changes. Improvements in model MJO teleconnection patterns may reduce the biases of other extratropical phenomena impacted by the MJO, such as the NAO, blocking, the PNA pattern, and others, potentially reducing uncertainties in how they will change in future climates. In addition, the focus of this study is MJO teleconnections in ocean-atmosphere coupled GCMs. A similar analysis utilizing AMIP GCM runs or weather forecasting models may provide further insight into the behavior of MJO teleconnections in those types of models.

Acknowledgments. We thank three anonymous reviewers for their insightful comments and suggestions. We are grateful to Masahiro Watanabe for providing the LBM used in this study and to Masato Mori for LBM code modifications for the propagating heat source. We also thank Haibo Liu and the Lamont-Doherty Earth Observatory for obtaining the CMIP5 data and the World Climate Research Programme's Working Group on Coupled Modelling, which is

responsible for CMIP. This work was supported by the National Science Foundation under Grant AGS-1441916, and the National Oceanic and Atmospheric Administration under Grants NA16OAR4310064 and NA15OAR4310099. SWS was funded by the Korea Meteorological Administration Research and Development Program under Grant KMIPA 2015-2100. This work was also funded in part by the National Science Foundation East Asia and Pacific Summer Institutes Fellowship Grant 1515489. The statements, findings, conclusions, and recommendations do not necessarily reflect the views of NSF or NOAA.

REFERENCES

- Adler, R., and Coauthors, 2003: The Version-2 Global Precipitation Climatology Project (GPCP) monthly precipitation analysis (1979–present). *J. Hydrometeorol.*, **4**, 1147–1167, doi:10.1175/1525-7541(2003)004<1147:TVGPCP>2.0.CO;2.
- Ahn, M.-S., and Coauthors, 2017: MJO simulation in CMIP5 climate models: MJO skill metrics and process-oriented diagnostics. *Climate Dyn.*, doi:10.1007/s00382-017-3558-4, in press.
- Alaka, G. J., and E. D. Maloney, 2012: The influence of the MJO on upstream precursors to African easterly waves. *J. Climate*, **25**, 3219–3236, doi:10.1175/JCLI-D-11-00232.1.
- Cassou, C., 2008: Intraseasonal interaction between the Madden-Julian oscillation and the North Atlantic Oscillation. *Nature*, **455**, 523–527, doi:10.1038/nature07286.
- Dawson, A., A. J. Matthew, and D. P. Stevens, 2011: Rossby wave dynamics of the North Pacific extra-tropical response to El Niño: Importance of the basic state in coupled GCMs. *Climate Dyn.*, **37**, 391–405, doi:10.1007/s00382-010-0854-7.
- Dee, D. P., and Coauthors, 2011: The ERA-Interim reanalysis: Configuration and performance of the data assimilation system. *Quart. J. Roy. Meteor. Soc.*, **137**, 553–597, doi:10.1002/qj.828.
- Donald, A., H. Meinke, B. Power, A. de H. N. Maia, M. C. Wheeler, N. White, R. C. Stone, and J. Ribbe, 2006: Near-global impact of the Madden-Julian oscillation on rainfall. *Geophys. Res. Lett.*, **33**, L09704, doi:10.1029/2005GL025155.
- Henderson, S. A., E. D. Maloney, and E. A. Barnes, 2016: The influence of the Madden-Julian oscillation on Northern Hemisphere winter blocking. *J. Climate*, **29**, 4597–4616, doi:10.1175/JCLI-D-15-0502.1.
- Hoskins, B. J., and D. J. Karoly, 1981: The steady linear response of a spherical atmosphere to thermal and orographic forcing. *J. Atmos. Sci.*, **38**, 1179–1196, doi:10.1175/1520-0469(1981)038<1179:TSLROA>2.0.CO;2.
- , and T. Ambrizzi, 1993: Rossby wave propagation on a realistic longitudinally varying flow. *J. Atmos. Sci.*, **50**, 1661–1671, doi:10.1175/1520-0469(1993)050<1661:RWPOAR>2.0.CO;2.
- Hsu, H.-H., 1996: Global view of the intraseasonal oscillation during northern winter. *J. Climate*, **9**, 2386–2406, doi:10.1175/1520-0442(1996)009<2386:GVOTIO>2.0.CO;2.
- Hung, M.-P., J.-L. Lin, W. Wang, D. Kim, T. Shinoda, and S. J. Weaver, 2013: MJO and convectively coupled equatorial waves simulated by CMIP5 climate models. *J. Climate*, **26**, 6185–6214, doi:10.1175/JCLI-D-12-00541.1.
- Jiang, X., and Coauthors, 2015: Vertical structure and physical processes of the Madden-Julian oscillation: Exploring key

- model physics in climate simulations. *J. Geophys. Res. Atmos.*, **120**, 4718–4748, doi:[10.1002/2014JD022375](https://doi.org/10.1002/2014JD022375).
- Jin, F., and B. J. Hoskins, 1995: The direct response to tropical heating in a baroclinic atmosphere. *J. Atmos. Sci.*, **52**, 307–319, doi:[10.1175/1520-0469\(1995\)052<0307:TDRTH>2.0.CO;2](https://doi.org/10.1175/1520-0469(1995)052<0307:TDRTH>2.0.CO;2).
- Jones, C., D. E. Waliser, K. M. Lau, and W. Stern, 2004: Global occurrences of extreme precipitation events and the Madden–Julian oscillation: Observations and predictability. *J. Climate*, **17**, 4575–4589, doi:[10.1175/3238.1](https://doi.org/10.1175/3238.1).
- Karoly, D., 1983: Rossby wave propagation in a barotropic atmosphere. *Dyn. Atmos. Oceans*, **7**, 111–125, doi:[10.1016/0377-0265\(83\)90013-1](https://doi.org/10.1016/0377-0265(83)90013-1).
- Kim, D., and Coauthors, 2009: Application of MJO simulation diagnostics to climate models. *J. Climate*, **22**, 6413–6436, doi:[10.1175/2009JCLI3063.1](https://doi.org/10.1175/2009JCLI3063.1).
- , A. H. Sobel, E. D. Maloney, D. M. W. Frierson, and I.-S. Kang, 2011: A systematic relationship between intraseasonal variability and mean state bias in AGCM simulations. *J. Climate*, **24**, 5506–5520, doi:[10.1175/2011JCLI4177.1](https://doi.org/10.1175/2011JCLI4177.1).
- , and Coauthors, 2014: Process-oriented MJO simulation diagnostic: Moisture sensitivity of simulated convection. *J. Climate*, **27**, 5379–5395, doi:[10.1175/JCLI-D-13-00497.1](https://doi.org/10.1175/JCLI-D-13-00497.1).
- Lau, W. K.-M., and D. E. Waliser, 2012: *Intraseasonal Variability in the Atmosphere–Ocean Climate System*. 2nd ed. Springer, 613 pp.
- Liebmann, B., H. H. Hendon, and J. D. Glick, 1994: The relationship between tropical cyclones of the western Pacific and Indian Oceans and the Madden–Julian oscillation. *J. Meteor. Soc. Japan*, **72**, 401–412.
- Lin, H., G. Brunet, and J. Derome, 2009: An observed connection between the North Atlantic Oscillation and the Madden–Julian oscillation. *J. Climate*, **22**, 364–380, doi:[10.1175/2008JCLI2515.1](https://doi.org/10.1175/2008JCLI2515.1).
- , —, and R. Mo, 2010: Impact of the Madden–Julian oscillation on wintertime precipitation in Canada. *Mon. Wea. Rev.*, **138**, 3822–3839, doi:[10.1175/2010MWR3363.1](https://doi.org/10.1175/2010MWR3363.1).
- Lorenz, D. J., and D. L. Hartmann, 2006: The effect of the MJO on the North American monsoon. *J. Climate*, **19**, 333–343, doi:[10.1175/JCLI3684.1](https://doi.org/10.1175/JCLI3684.1).
- Madden, R. A., and P. Julian, 1971: Detection of a 40–50 day oscillation in the zonal wind in the tropical Pacific. *J. Atmos. Sci.*, **28**, 702–708, doi:[10.1175/1520-0469\(1971\)028<0702:DOADOI>2.0.CO;2](https://doi.org/10.1175/1520-0469(1971)028<0702:DOADOI>2.0.CO;2).
- , and —, 1972: Description of a global-scale circulation cells in the tropics with a 40–50 day period. *J. Atmos. Sci.*, **29**, 1109–1123, doi:[10.1175/1520-0469\(1972\)029<1109:DOGSCC>2.0.CO;2](https://doi.org/10.1175/1520-0469(1972)029<1109:DOGSCC>2.0.CO;2).
- Maloney, E. D., and D. L. Hartmann, 2000: Modulation of eastern North Pacific hurricanes by the Madden–Julian oscillation. *J. Climate*, **13**, 1451–1460, doi:[10.1175/1520-0442\(2000\)013<1451:MOENPH>2.0.CO;2](https://doi.org/10.1175/1520-0442(2000)013<1451:MOENPH>2.0.CO;2).
- , and S.-P. Xie, 2013: Sensitivity of tropical intraseasonal variability to the pattern of climate warming. *J. Adv. Model. Earth Syst.*, **5**, 32–47, doi:[10.1029/2012MS000171](https://doi.org/10.1029/2012MS000171).
- Matthews, A. J., B. J. Hoskins, and M. Masutani, 2004: The global response to tropical heating in the Madden–Julian oscillation during the northern winter. *Quart. J. Roy. Meteor. Soc.*, **130**, 1991–2011, doi:[10.1256/qj.02.123](https://doi.org/10.1256/qj.02.123).
- Mori, M., and M. Watanabe, 2008: The growth and triggering mechanisms of the PNA: A MJO–PNA coherence. *J. Meteor. Soc. Japan*, **86**, 213–236, doi:[10.2151/jmsj.86.213](https://doi.org/10.2151/jmsj.86.213).
- Rashid, H. A., H. H. Hendon, and M. C. Wheeler, 2011: Prediction of the Madden–Julian oscillation with the POAMA dynamical prediction system. *Climate Dyn.*, **36**, 649–661, doi:[10.1007/s00382-010-0754-x](https://doi.org/10.1007/s00382-010-0754-x).
- Riddle, E. E., M. B. Stoner, N. C. Johnson, M. L. L’Heureux, D. C. Collins, and S. B. Feldstein, 2013: The impact of the MJO on clusters of wintertime circulation anomalies over the North American region. *Climate Dyn.*, **40**, 1749–1766, doi:[10.1007/s00382-012-1493-y](https://doi.org/10.1007/s00382-012-1493-y).
- Sardeshmukh, P. D., and B. J. Hoskins, 1988: The generation of global rotational flow by steady idealized tropical divergence. *J. Atmos. Sci.*, **45**, 1228–1251, doi:[10.1175/1520-0469\(1988\)045<1228:TGOGRF>2.0.CO;2](https://doi.org/10.1175/1520-0469(1988)045<1228:TGOGRF>2.0.CO;2).
- Seo, K.-H., and S.-W. Son, 2012: The global atmospheric circulation response to tropical diabatic heating associated with the Madden–Julian oscillation during northern winter. *J. Atmos. Sci.*, **69**, 79–96, doi:[10.1175/2011JAS3686.1](https://doi.org/10.1175/2011JAS3686.1).
- , H.-J. Lee, and D. M. W. Frierson, 2016: Unraveling the teleconnection mechanisms that induce wintertime temperature anomalies over the Northern Hemisphere continents in response to the MJO. *J. Atmos. Sci.*, **73**, 3557–3571, doi:[10.1175/JAS-D-16-0036.1](https://doi.org/10.1175/JAS-D-16-0036.1).
- Taylor, K. E., R. J. Stouffer, and G. A. Meehl, 2012: An overview of CMIP5 and the experiment design. *Bull. Amer. Meteor. Soc.*, **93**, 485–498, doi:[10.1175/BAMS-D-11-00094.1](https://doi.org/10.1175/BAMS-D-11-00094.1).
- Ting, M., and P. D. Sardeshmukh, 1993: Factors determining the extratropical response to equatorial diabatic heating anomalies. *J. Atmos. Sci.*, **50**, 907–918, doi:[10.1175/1520-0469\(1993\)050<0907:FDTERT>2.0.CO;2](https://doi.org/10.1175/1520-0469(1993)050<0907:FDTERT>2.0.CO;2).
- Vecchi, G. A., and N. A. Bond, 2004: The Madden–Julian oscillation (MJO) and northern high latitude wintertime surface air temperatures. *Geophys. Res. Lett.*, **31**, L04104, doi:[10.1029/2003GL018645](https://doi.org/10.1029/2003GL018645).
- Waliser, D., and Coauthors, 2009: MJO simulation diagnostics. *J. Climate*, **22**, 3006–3030, doi:[10.1175/2008JCLI2731.1](https://doi.org/10.1175/2008JCLI2731.1).
- Watanabe, M., and M. Kimoto, 2000: Atmosphere–ocean thermal coupling in the North Atlantic: A positive feedback. *Quart. J. Roy. Meteor. Soc.*, **126**, 3343–3369, doi:[10.1002/qj.49712657017](https://doi.org/10.1002/qj.49712657017).
- Weare, B. C., 2013: El Niño teleconnections in CMIP5 models. *Climate Dyn.*, **41**, 2165–2177, doi:[10.1007/s00382-012-1537-3](https://doi.org/10.1007/s00382-012-1537-3).
- Wheeler, M. C., and H. H. Hendon, 2004: An all-season real-time multivariate MJO index: Development of an index for monitoring and prediction. *Mon. Wea. Rev.*, **132**, 1917–1932, doi:[10.1175/1520-0493\(2004\)132<1917:AARMMI>2.0.CO;2](https://doi.org/10.1175/1520-0493(2004)132<1917:AARMMI>2.0.CO;2).
- Wolding, B. O., E. D. Maloney, and M. Branson, 2016: Vertically resolved weak temperature gradient analysis of the Madden–Julian oscillation in SP-CESM. *J. Adv. Model. Earth Syst.*, **8**, 1586–1619, doi:[10.1002/2016MS000724](https://doi.org/10.1002/2016MS000724).
- Yanai, M., S. Esbensen, and J.-H. Chu, 1973: Determination of bulk properties of tropical cloud clusters from large-scale heat and moisture budgets. *J. Atmos. Sci.*, **30**, 611–627, doi:[10.1175/1520-0469\(1973\)030<0611:DOBPOT>2.0.CO;2](https://doi.org/10.1175/1520-0469(1973)030<0611:DOBPOT>2.0.CO;2).
- Yasui, S., and M. Watanabe, 2010: Forcing processes of the summertime circumglobal teleconnection pattern in a dry AGCM. *J. Climate*, **23**, 2093–2114, doi:[10.1175/2009JCLI3323.1](https://doi.org/10.1175/2009JCLI3323.1).
- Yoo, C., S. Park, D. Kim, J.-H. Yoon, and H.-M. Kim, 2015: Boreal winter MJO teleconnection in the Community Atmosphere Model version 5 with the unified convection parameterization. *J. Climate*, **28**, 8135–8150, doi:[10.1175/JCLI-D-15-0022.1](https://doi.org/10.1175/JCLI-D-15-0022.1).